© [2013]

Andrea Shilling

ALL RIGHTS RESERVED

CHARACTERIZATION OF GROUNDWATER DISCHARGE SITES USING REMOTE SENSING AND WETLAND CORES, LAKE EYASI BASIN, TANZANIA

By

ANDREA M. SHILLING

A thesis submitted to the

Graduate School – New Brunswick

Rutgers, The State University of New Jersey

In partial fulfillment of the requirements

for the degree of

Master of Science

Graduate Program in Geological Sciences

Written under the direction of

Dr. Gail M. Ashley

_____

and approved by

_____

_____

_____

New Brunswick, New Jersey

January, 2013

ABSTRACT OF THESIS

Characterization of groundwater discharge sites using remote sensing and wetland cores, Lake Eyasi basin, Tanzania

By ANDREA M. SHILLING

Thesis Director:

Dr. Gail M. Ashley

Lakes in arid regions commonly dry up creating gaps in the sediment records. Groundwater discharge (GWD) sites are sourced from aquifers that may be recharged, at great distances and unaffected by local precipitation levels. GWD occurs as surface springs and seeps supporting continuously aggrading wetlands with the potential to record environmental and climatic change.

The study site is the NE margin of Lake Eyasi in the Eastern Gregory Rift of Northern Tanzania. Landsat and GoogleEarth images were analyzed to locate GWD. In July 2011 sites were visited and 7 cores collected. All cores underwent initial analyses (magnetic susceptibility, density, and physical description), and Core 1A selected for radiocarbon dating and sedimentological, geochemical, and biological analysis. All cores contained 2 intervals distinguishable by color and content. The base of the upper interval (28-29 cm depth) of Core 1A was AMS dated to 270 +/- 30 yrs BP (conventional radiocarbon age) using seeds.

The lower interval, light (Munsell: 5Y 4/1) organic-poor clay, impoverished microfauna, 5% organic matter, low total organic carbon (</= 1%) and total nitrogen (<0.1%), and average TOC/TN of ~11.4. The upper interval, darker (Munsell: 10YR 2/1)

organic-rich, microfauna consisting of diatoms and testate amoebae, 10-35% organic matter, total organic carbon 3-22% and total nitrogen 0.2-1.2%, and average TOC/TN of ~14.5.

The lower interval records pre-wetland, lake margin sedimentation, while the upper interval is a freshwater wetland deposit. Contact between intervals represents onset of groundwater flow to the site. When calibrated to calendar years the age date indicates GWD reached the site between 200-500 years before today (2012). When the groundwater travel time, estimated to be 400 years, is factored in the date of the rainfall responsible for recharging groundwater coincides with the start of the Little Ice Age, a period of increased rainfall in East Africa.

This study shows GWD sites contain usable climate records. Additionally, remote sensing offers a low-cost way to identify and monitor GWD, critical in arid regions where GWD means potable water. Lastly, radiocarbon dating shows these sites are not ephemeral features and have the capacity to persist for hundreds of years.

ACKNOWLEDGEMENTS

First I'd like to thank my advisor, Dr. Gail Ashley, Rutgers University, whose infinite wisdom, guidance, and patience throughout this process was critical and always appreciated. Thank you to my committee members, Dr. Craig Feibel and Dr. Ying Fan Reinfelder of Rutgers University and Dr. Michelle Goman of Sonoma State College for their numerous suggestions and assistance over the last couple of years. A special thank you to Michelle for showing me my first testate amoebae (!!) and then showing me how to find my own and for the many emails as I attempted to identify the species of testate amoebae, thank you for your patience!

This research would not have been possible without funding from a Rutgers New Brunswick Graduate School pre-dissertation award and Dr. Ashley's grant money, which helped cover field expenses making this whole thesis possible.

There are numerous collaborators who ran and analyzed samples that I must thank. Dr. Bernhart Owen, of the Hong Kong Baptist University, for running and analyzing the diatom samples (and so quickly!). Clayton Magill, of Penn State, who ran the n-alkane specific isotope analysis. Doris Barboni, of CEREGE: Centre Européen de Recherche et d'Enseignement des Géosciences de l'Environnement, who will be performing the pollen and phytolith analysis in the near future.

Thanks to Dr. Rick Lathrop director of the Center for Remote Sensing and Spatial Analysis (CRSSA) at Rutgers University for teaching me the ways of ERDAS Imagine and patiently answering all my questions. Many thanks to Dr. Dave Finkelstein at the University of Massachusetts-Amherst for helping me (and allowing me!) to run my carbon and nitrogen elemental analysis and isotope samples (last minute) and getting the

results to me in time for GSA thank you, thank you, thank you. (Much appreciation to the isotope lab for providing me a spot to write my thesis in peace.) Special thanks to Dr. Isla Castañeda for all the guidance and patience while letting me finish up my master's while simultaneously starting my PhD, very much appreciated! Thank you to the staff at LacCore for all the help analyzing my "baby" cores and to Beta Analytic for determining the ages of my samples in a timely manner. To all those who assisted in field work, including the Schmelling family of Kisima Ngeda for providing a camping site/home base, and to Dr. Henry Bunn and his students for all the good times in the field, many thanks!

A special thank to my cousin Catherine whose many hours of assistance (and company) in the lab helped immensely! To Margot and Linda for listening, and all of the graduate students who were at Rutgers while I was, thank you all for everything and all the good memories!! And finally, most importantly to my family and all my friends who've helped me stay focused and positive during this experience your support means everything, I am deeply grateful, much thanks.

TABLE OF CONTENT

Page

Title Page …… i

Abstract ……... ii

Acknowledgements……. iv

Table of Content……. vi

List of Figures ……..…… x

List of Tables……. xii

Introduction…….... 1

Background……..… 6

Geology……... 6

North Tanzanian Divergence…….. 7

Gregory Rift……..... 9

Eyasi Basin…….……. 10

Climate…… 14

Modern Climate…….…….…….

Field Methods ……..……. 32

Site Description…….……. 32

Core Collection……..……. 32

Lab Methods……..…. 34

Sedimentology…….……. 34

Initial Description……..……. 34

Sub-sampling…….……. 36

Percent Sand……..……. 36

Sedimentation Rate…….……..……. 38

Geochemical Analysis…….…..……. 38

Sequential Loss On Ignition …….…….……..... 38

TOC and TN Bulk Element and Isotopic Analysis…… 39

N-alkane Isotopic Analysis ….....……. 40

Biological Analysis…….…….……..…...…..…….…….. 40

Seed-picking……..……. 40

Diatoms……..…… 40

Testate Amoebae…… 41

Radiocarbon dating……. 41

Results…… 42

Remote Sensing…….……. 42

Sedimentology…….…….……. 42

Core description……. 42

Density……..……. 43

Magnetic Susceptibility……. 43

Percent Sand…….……..……..……. 48

Sedimentation Rate…….……..…….. 51

Geochemical Analysis…….…….……. 51

Sequential LOI……..……. 51

TOC – Elemental Analysis……. 51

TN – Elemental Analysis……..……. 53

TOC/TN Ratio……...……. 53

Carbon Stable Isotope…….……..……. 56

Nitrogen Stable Isotope……..……. 56

N-alkane Isotopic Analysis ……..…..…… 56

Biological Analysis…….…….…….……..……..…….. 58

Diatoms…….……. 58

Testate Amoebae……...……. 58

Radiocarbon Dating…….…….……..……..…….. 61

Radiocarbon Dates…….……. 61

Discussion…….……. 61

Remote Sensing…….……. 61

Groundwater Discharge Onset ……..……. 64

Wetland Development ……..……. 66

Sub-interval of Increased Salinity...……..……. 67

Future Research ……..……..……. 67

Conclusions……..…….. 68

References……. 72

Appendices……. 80

Appendix 1 – Old topographic Map……..……. 80

Appendix 2 – Landsat Image list…….……..…. 81

Appendix 3 – Core Photographs…….……...……. 85

Appendix 4 – N-alkane methods……...……. 86

Appendix 5 – Density plots…… 99

Appendix 6 – Magnetic Susceptibility plots……..…….……... 100

Appendix 7 – N-alkane plots……..…… 101

Appendix 8 – Beta Analytic Report…….….. 102

Appendix 9 – Groundwater Travel Time Calculations……..… 105

Figure List		Page #
Fig 1	Groundwater flow conceptual model	3
Fig 2	Structural map – North Tanzanian Div.	8
Fig 3	Structural cross section	11
Fig 4	Structural Overview map	12
Fig 5	East and West Eyasi Basin Structure	13
Fig 6	Vegetation photographs	20
Fig 7	Wildlife photographs	21
Fig 8	Topographic map	23
Fig 9	N-alkanes	28
Fig 10	Coring photographs	35
Fig 11	Sub-sampling diagram	37
Fig 12	NDVI results	44
Fig 13	GoogleEarth study	45
Fig 14	Core description, Core 1A	46
Fig 15	Density plot, Core 1A	47
Fig 16	Magnetic susceptibility, Core 1A	49
Fig 17	Percent sand, Core 1A	50
Fig 18	Percent organic matter, Core 1A	52
Fig 19	% TN and % TOC, Core 1A	54
Fig 20	TOC/TN plot, Core 1A	55
Fig 21	Carbon and Nitrogen stable isotope plots, Core 1A	57

Fig 22	N-alkane plots, Core 1A	59
Fig 23	Diatom Analysis, Core 1A	60
Fig 24	Testate Amoebae, Core 1A	62

Table List		Page #
Table 1	Landsat mission dates	24
Table 2	MSS bad designations	25
Table 3	TM and ETM+ band designations	27
Table 4	GPS location of core sites	33

INTRODUCTION

Freshwater wetlands commonly occur in the arid to semi-arid regions of East Africa (Thompson and Hamilton, 1983; Crafter et al., 1992; Hughes and Hughes, 1992; Deocampo, 2002; Ashley et al., 2013), and while many are short-lived ephemeral features, others are relatively long-lived groundwater (GW) fed features. These GW-fed wetlands are an important part of hydrologically closed basins like those of the East African Rift due to their ability to persist despite arid conditions (Deocampo, 2002; Liutkus and Ashley, 2003; Ashley et al., 2004; Deocampo, 2005; Ashley et al., 2013). Geologic structures such as faults or bedrock fractures providing a pathway for GW flow to reach the surface at these groundwater discharge (GWD) sites (Rosen, 1994; Quade et al., 1995; Deocampo, 1997; Deocampo and Ashley, 1999; Renaut and Jones, 2000; Ashley 2001a; Deocampo, 2002; Deocampo, 2005; Ashley et al., 2013).

In the hydrologically closed basins of East Africa climate change can produce lake-level fluctuations that expose large areas of low-gradient lake margin (Kutzbach and Street-Perrott, 1985; Deocampo, 2002; Deocampo, 2005). Lake margin is defined as the area between a standing body of water and the adjacent terrestrial environment (Feibel, 2001). This region is often sparely vegetated if not bare. It is on these expanses of lake margin that GWD occurs and eventually wetlands develop and are supported by continuously flowing groundwater (Ashley, 2001a; Deocampo, 2002; Deocampo, 2005). The initiation of these GWD features can either be tectonic or climate related (Deocampo, 2002). Tectonic activity may cause a shift in sediment layers, move a fault, or cause some other change in the sediment or bedrock opening up a new pathway for GWD (Deocampo, 2002). Climate can also cause GWD features to form due to the close

relationship between lake-margin wetlands and regional hydrology (Deocampo, 2002). If groundwater discharge occurs during high lake level, it enters directly into the lake water. The GWD features can only exist when the lake level and thus water table is low enough that the lake margin is exposed (Deocampo, 2002). For this situation to occur evaporation and evapotranspiration must be greater than precipitation (Deocampo, 2002).

The GWD and associated wetlands that are the focus of this study are found along the margin of Lake Eyasi in the Eyasi Basin of Northern Tanzania. The Eyasi Basin is a half graben within the Gregory Rift Valley of northern Tanzania, part of the East African Rift System (EARS) (Deocampo, 2002; Deocampo, 2005; Dawson, 2008). Springs and associated wetlands, here referred to as GWD sites, were previously studied on the NE margin of the basin (Deocampo, 2002; Deocampo, 2005). The hydrologic model explaining the GWD is based on fundamental hydrologic principles (Figure 1) (Ashley et al., 2013). Precipitation moves from local topographic highs through the subsurface toward topographic lows and emerge as springs at faults or at the base of slopes. The Ngorongoro Volcanic Highlands, a 2500 meter high massive, north of Eyasi is the likely moisture source for the basin's groundwater (Deocampo, 2002; Deocampo, 2005). Studies of groundwater-fed systems in other EARS basins (Deocampo, 2002; Ashley et al., 2004; Deocampo, 2005; Johnson et al., 2009) suggest these springs are sourced by aquifers and are thus able to persist in arid conditions. A number of multi-proxy studies have shown that sediment captured in the wetlands associated with GWD provide high-resolution paleoclimate information, which is possible to date via AMS radiocarbon dating (Deocampo, 2002; Deocampo, 2005; Ryner et al., 2008; Rucina et al., 2010).

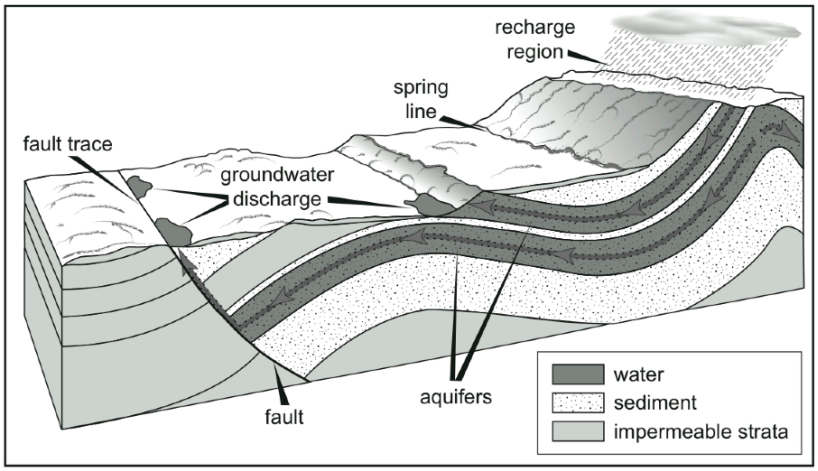

Figure 1. Diagram from Ashley et al. (2013) showing possible ways to explain groundwater discharge that occurs at the base of slopes. In the case of the GWD sites studied at Lake Eyasi, rain falls on the Ngorongoro Volcanic Highlands and discharges along the NE margin of the lake.

A previous study of the groundwater-fed wetlands on the margin of Eyasi found complex relationships among the many factors impacting sedimentation; these factors include: clastic sedimentation, mineral precipitation and diagenesis, bioturbation, peat formation, and vegetative sediment trapping (Deocampo, 2002). Additionally, tectonics and climate not only cause the initiation of GWD but also impact sedimentation by means of sediment supply, aqueous geochemistry, large-mammal activity, and patterns of vegetation to name a few (Deocampo, 2002). It is the dynamic and complex interactions amongst the factors that can complicate the interpretation of groundwater-fed wetland deposits.

Typically a stratigraphic relationship exists between the lake margin wetland deposits and pre-wetland lacustrine or lake margin deposits (Ashley, 2001a; Deocampo, 2002; Deocampo, 2005). This relationship often provides a high-resolution, datable means of identifying paleoenvironmental and paleoclimate changes (Ashley, 2001a,b; Deocampo, 2002; Deocampo, 2005). The low gradient of lake margins means that sediment, both allochthonous and autochthonous easily accumulate producing an organic rich record (Ashley et al., 2013). Many multi-proxy studies have been performed wetland deposits (Deocampo, 2002; Deocampo, 2005; Ryner et al., 2008; Rucina et al., 2010) and the results of these studies demonstrate that wetlands represent important databases of information not only about current but also past climate and hydrologic conditions in Africa (Thompson and Hamilton, 1983; Deocampo, 2002; Ashley et al., 2013).

The importance of these groundwater-fed wetlands goes far beyond their ability to contain climate and/or hydrologic records (Ashley et al., 2004). As noted by numerous

climate studies, the East African region has been experiencing increasing aridity resulting in famines, threatening the lives of livestock and humans alike (Hughes and Hughes, 1992; Lamb et al., 2003; Kiage and Liu, 2006; Kiage and Liu, 2009; Rucina et al., 2010). Haack et al., (1996) report that water table levels in East Africa have been steadily dropping over the past few decades causing once permanent water sources to decrease in size and disappear. To address this issue numerous recent conferences and projects, e.g. the conference in 2008 on Groundwater & Climate in Africa, have focused on addressing the growing water crisis and subsequent crop shortage in East Africa (Taylor et al., 2009). The more recently formed Mawari Project focuses on sustainable management of water resources in the EARS (www.mawari.net). The ongoing drought and subsequent food shortages have increased interest in the potential of groundwater as a reliable source of potable water and resulted in a call for more information on GWD.

Determining the longevity of GWD sites in this arid region is a crucial part of this study. For the people of this region it is important to know if the water sources can be relied on for only a couple of years or potentially hundreds or more. In addition to the needs of modern people, the longevity of these features could provide a modern analog for the paleoenvironmental record of pre-historic archaeological sites and thus insight into the lives of early man. The Tanzanian segment of the East African Rift System has a rich history in hominin evolution (Olduvai Gorge and Laetoli) (Leakey, 1971; Leakey and Hay, 1979). Research at Olduvai Gorge has revealed that many of the archaeological sites are associated with springs, wetlands and woodlands (Ashley et al., 2010 a, b). Thus understanding what are likely modern analogs of these ancient sites could provide information regarding permanent sources of water available to early humans. While the

spring systems examined as part of this study have clearly not been around since the time of early man, similar features existed and may have been utilized by them. Identifying whether or not these springs persist long enough to be a reliable source of water in today's arid climate may help explain how early humans coped with arid conditions and droughts.

The objectives of this study are: (1) Locate GWD within the Eyasi Basin via remote sensing; (2) Ground truth logistically feasible sites and collecting sediment cores; and (3) Analyze cores: determine age of sediments using radiocarbon and interpret the wetlands' climate history with geochemistry and biological remains. The hypotheses include: (1) Groundwater, protected from evaporation, is able to support wetlands and provide dependable, long-term (multi-decadal or more) sources of potable water. (2) GWD able to support wetland vegetation is identifiable through remote sensing. (3) The organic-rich wetland sediments have the potential to preserve sedimentation and paleoclimate records.

BACKGROUND

Geology

The 4,000 km East African Rift System (EARS) has long been a focus of scientific research for the opportunity it provides to study continental rifting (McConnell, 1972; Dawson, 2008). The EARS has both an eastern and western branch, which appear to "wrap around" the Archaean Tanzanian craton, instead following the Proterozoic mobile belts (Ring et al., 2005; Dawson, 2008). The eastern branch, which follows the north to south trend of the Mozambique orogenic fold belt, is characterized by greater

amounts of magmatism and rift associated volcanism that has moved southwards with time (Dawson, 2008). Within the eastern branch of the EARS is the Gregory Rift, which contains a connected string of rift basins trending north to south from south-west Ethiopia into Tanzania (Ebinger et al., 1997) and many would even extend the Gregory Rift to Lake Malawi (Bosworth et al., 1992; Frostick 1997).

North Tanzanian Divergence

Unlike the majority of the EARS system, the Eyasi and Manyara rifts in northern Tanzania transect the intersection of the Archaean Tanzanian craton and the Proterozoic mobile belts (Ring et al., 2005). The Eyasi and Manyara rifts are in a region known as the northern Tanzanian Divergence Zone, and an area of particular interest in many structural and seismic studies (Ring et al., 2005). In this region of the EARS the rift expands from 50-60 km wide in southern Kenya to 200 km [Ring et al. (2005) reports the rift as being 300-400 km wide] in northern Tanzania (Ebinger et al., 1997, Foster et al., 1997) (Figure 2). One of the theories for the width change of this section of the EARS is the difference in lithospheric structure between the Archaean Tanzanian craton and the Proterozoic Mozambique belt (Ebinger et al., 1997; Foster et al., 1997; Dawson, 2008). The sheared contact between the Archaean Tanzanian craton and Proterozoic Mozambique belt cuts across and is exposed in the Eyasi Basin (Foster et al., 1997).

In addition to the change in rift width, the Tanzanian Divergence also differs from southern Kenya in general basin morphology. In Kenya the rifts have major faults on either side of the basins, in contrast, those in the Tanzanian Divergence have only one major fault bounding the western side of the basin, giving them a half graben morphology (Dawson, 2008).

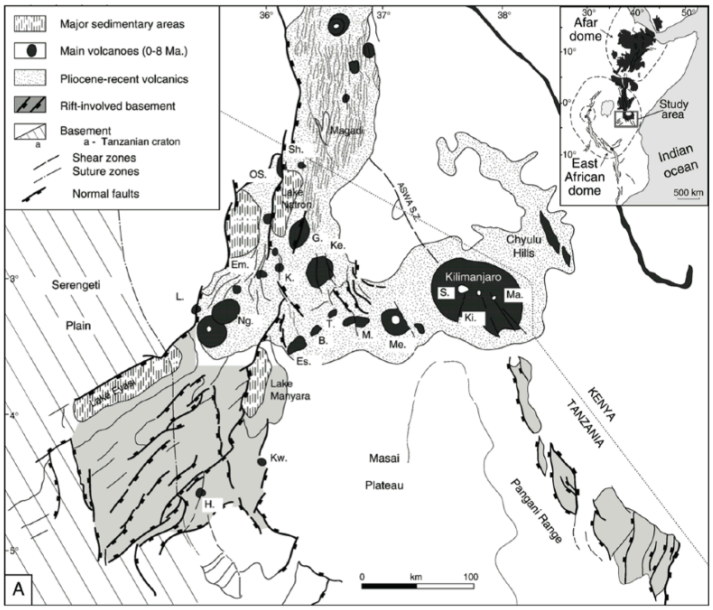

Figure 2. Structural map of the Northern Tanzanian Divergence. Figure from Le Gall et al. (2008).

Recently the North Tanzanian Divergence has come to be considered a two-armed rift pattern composed of: (1) The Eyasi and Manyara fault systems in the west and (2) the Pangani rift system to the east (Le Gall et al., 2008). The Eyasi and Manyara faults are part of the Mbulu region, a wide area of tilted fault blocks to the western side of the divergence (Le Gall et al., 2008). These faults represent a continuation of the Natron trough, however their morphology differs, thought to be a result of the faulting cutting through the Archaean Tanzanian craton (Le Gall et al., 2008). Both the Eyasi and Manyara basins have the half graben morphology mentioned previously (Foster et al., 1997; Le Gall et al., 2008). In contrast, the Pangani fault to the east bears more resemblance to the faults in southern Kenya, again most likely due to the fact that the Pangani fault does not cut through the craton but rather only through the Mozambique belt like the faults in Kenya (Le Gall et al., 2008).

Within the North Tanzanian Divergence lies the Ngorongoro Volcanic Highland (Frostick, 1997; Gawthorpe and Leeder, 2000). This complex of roughly 9 volcanoes includes the Ngorongoro Crater, Oldeani, and Oldoinyo Lengai (carbonate volcano) (Frostick, 1997; Gawthorpe and Leeder, 2000). For the areas within the North Tanzanian Divergence, the Ngorongoro Volcanic Highland represents the local high and moisture source for many regions (Frostick, 1997; Gawthorpe and Leeder, 2000).

Gregory Rift

The portion of the Gregory Rift in northern Tanzania is characterized by large-scale extensional block faulting beginning ~30 Ma, however most subsidence has occurred in the last 4 Ma (Hay, 1976; Williams, 1978; Baker, 1986). The active zone of extension within the Gregory Rift includes the Pangani Rift, the Manyara rift, and the

Eyasi Rift (Dawson, 1992; Foster et al., 1997). The general basin structure within the northern Tanzanian Divergence Zone is basin bounded on the western side by major border faults and on the eastern side by mostly unfaulted basement flexural warp (Foster et al., 1997). The border faults bounding the basins to the west, forming rift escarpments, are steeply dipping planar normal fault systems (Foster et al., 1997). The typical throw on the border faults is >500 m with uplifted flanks (Foster et al., 1997). Basins in this region typically have small amounts of synrift deposits, less than 3 km, which suggests cumulative extension was minor across the basins (Ring et al., 2005).

Eyasi Basin

Regionally volcanic rocks range from basaltic to trachytic lavas as well as trachyandesitic volcaniclastics (Hay, 1976; Williams, 1978). The volcano bordering the northeast margin of Lake Eyasi, Oldeani Mountain, is a deeply incised Neogene trachyandesitic volcano (Hay, 1976; Williams, 1978). The lake lies in a half graben to the east of the Hamwawa Escarpment formed by the Eyasi fault and to the southwest of the Ngorongoro Volcanic Highlands (Hay, 1976; Williams, 1978) (Figure 3).

The Eyasi basin measures approximately 100 km by 30 km and runs in a southwest direction from below the Neogene Crater Highlands to the Iramba Plateau (Foster et al., 1997) (Figure 4). Utilizing seismic and gravity data, Ebinger et al. (1997), identified a higher region of basement separating the Eyasi Basin into two sub-basins: East Eyasi Basin and West Eyasi Basin. The East Eyasi Basin is bounded to the west by the Eyasi fault while the West Eyasi Basin is bounded to the south-east by the Iramba Plateau (Ebinger et al., 1997) (Figure 5).

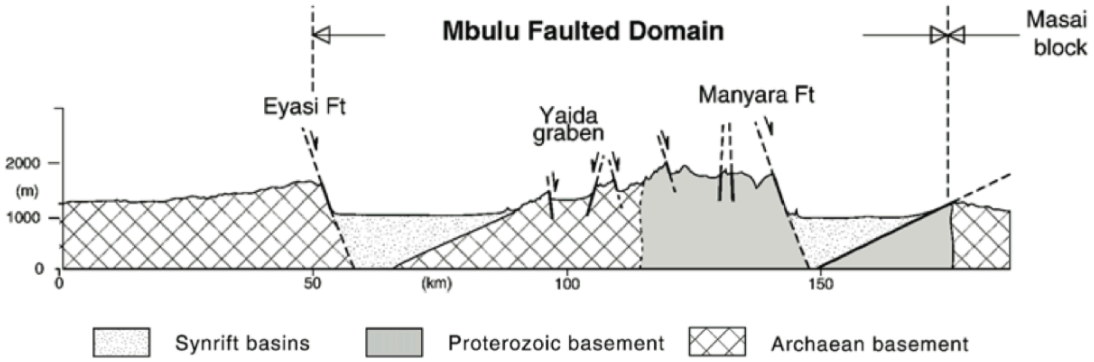

Figure 3. Structural cross section through the Mbulu plateau with a vertical exaggeration of roughtly 10 meters. Figure from Le Gall et al. (2008).

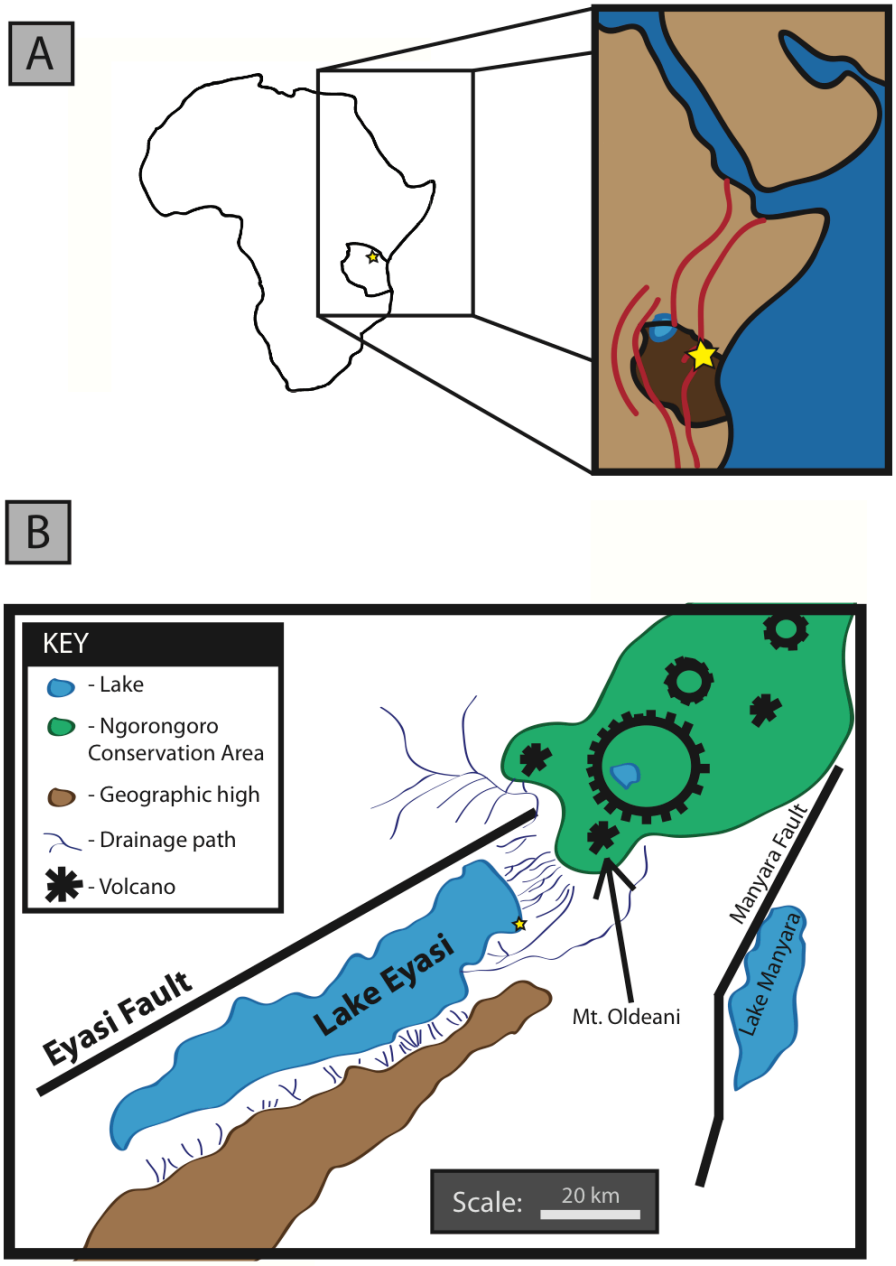

Figure 4. (A) Map of Africa with Tanzania outlined and a yellow star indicating field site. Inset map shows location of field site (yellow star) within the East African Rift System (approximate location of major rift boundaries shown in red). (B) Close up map of Eyasi Basin, yellow star marks field site on lake margin.

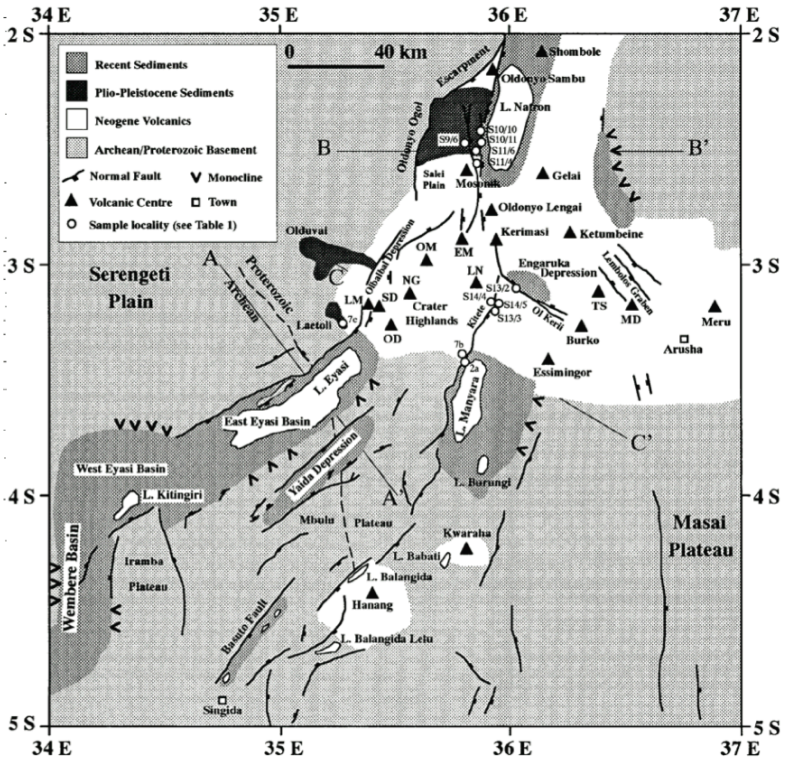

Figure 5. Map showing location of East and West Eyasi Basin as well as structure, surface geology, and volcanic centers in the region. Figure from Foster et al. (1997). Volcanoes indicated by letters: EM = Embagai; OM = Olmoti; LN = Loolmalasin; NG = Ngorongoro; SD = Sadiman; LM = Lemagrut; OD = Oldeani; TS = Tarosero; MD = Monduli.

The East Eyasi Basin (EEB) is bounded on the west by the Eyasi fault, giving the Eyasi Basin its asymmetrical half graben morphology (Foster et al., 1997). The Eyasi fault is a single fault segment approximately 100 km long, with greatest occurrence of cross fault throw near the basin's center and decreasing to zero at the south-west end (Foster et al., 1997). The Eyasi Rift system cuts through both Archaean and Late Proterozoic crust/ Mozambique orogenic fold belt (Ebinger et al., 1997). The amount of synrift deposition has been determined to be no greater than 2 km thick within the basin (Ebinger et al., 1997).

To the north of Lake Eyasi is Oldeani, one of the numerous volcanoes making up the Ngorongoro Volcanic Highland. The deposits from Oldeani have been found to be silica saturated, ranging from basalt to trachyandesite (Mollel et al., 2011). The texture of the deposits is fine-grained phaneritic to aphenitic, occasionally porphyritic and scoriaceous (Mollel et al., 2011). The mineral assemblages of the deposits include plagioclase, augite, olivine, and titanomagnetite (Mollel et al., 2011). $^{40}Ar/^{39}Ar$ age dating revealed Oldeani to be roughly 1.5 Ma, making it one of the youngest volcanoes in the Ngorongoro complex (Mollel et al., 2011).

Climate

Modern Climate

The general climate of East Africa is sub-arid to sub-humid, with the Eyasi Basin being sub-arid (Kiage and Liu, 2006). Rainfall in the Eyasi region is bimodal, with the long rains occurring from March to May and a shorter period of rain from October to November (Nicholson, 1996; Nicholson, 2000; Kiage and Liu, 2006). There are three major air streams, the Congo air (W-SW flow), the NE monsoon, and the SE monsoon,

which control the region's climate making it one of the most complex in Africa (Nicholson, 1996; Nicholson, 2000; Kiage and Liu, 2006). Where these air masses collide three convergence zones form; the ITCZ (separating the two monsoons) and the Congo Air Boundary (separating easterlies and westerlies) are both surface convergence zones, while the third zone is higher in the atmosphere, separating northern and southern flows (Nicholson, 1996; Nicholson, 2000; Kiage and Liu, 2006). All these factors acting on the region's climate can make it difficult to discern the driving force behind the climate at a specific site and specific time in history (Nicholson, 1996; Nicholson, 2000; Kiage and Liu, 2006).

Rainfall on the Ngorongoro Volcanic Highlands, to the north of Lake Eyasi, averages 1200 mm/yr (Deocampo, 2002; Deocampo, 2005), while in Eyasi Basin rainfall is about half that, between 500-600 mm/yr (Hughes and Hughes, 1992). If more water were available for evapotranspiration the rates for the region would be roughly 2500 mm/yr, which would result in a negative water budget where evapotranspiration exceeds precipitation. As a result of such high evapotranspiration rates there is a lack of surface water such as streams/rivers and the lakes in this region tend to be saline alkaline such as lake Eyasi (Rowntree, 1989). Regional prevailing winds are from the east blowing westward, however the Ngorongoro Volcanic Highland and Eyasi Basin produce a local effect causing thermal convection so locally wind moves from north to south.

Holocene climate

Little is understood about the mechanisms governing the climate and hydrologic changes observed in tropical and subtropical Africa both today and in the paleo-record (Johnson et al., 2002; Schefuβ et al., 2011) and as a result much of what is observed in

the paleo-record is not fully understood. Africa's large size and varying landscape both act to further complicate the climate of this continent (Johnson et al., 2002). The Holocene represents the last 10,000 years of a 20,000-year Precession cycle, and is a time of decreasing insolation (deMenocal et al., 2000). This has resulted in a wet to dry shift in the tropics and a warm to cool shift in temperate regions (deMenocal et al., 2000). Superimposed on this broad trend are sub-Milankovitch fluctuations relating to interactions between the atmosphere and ocean circulation systems (deMenocal et al., 2000). While the climate in more recent times (<2,000 years BP) may seem quite variable to some, many see the last 2000 years as stable and uneventful when compared with the climate during the early and middle Holocene (Verschuren, 2004; Russell et al., 2007; Russell and Johnson, 2007).

The African humid period (~11-4 ka) is generally thought to be a time of warmer and wetter conditions (Thompson et al., 2002) however as with most climate studies the extent and impact of this climate change vary regionally. The Medieval Climate Anomaly (MCA) (~1000 – 700 BP / ~ AD 1000-1270) is considered a time of drier climate within the East Africa Rift System (Mohammed et al., 1995; Verschuren et al., 2000) and the Little Ice Age (LIA) (~730 – 150 BP / ~ AD 1270-1850), though punctuated by three episodes of drier climate, was overall wetter (Verschuren et al., 2000; Verschuren, 2001, Ashley et al., 2004). These prolonged dry episodes occurred at AD 1380-1420, 1560-1620, and 1760-1840 (Verschuren et al., 2000). As is often the case within Africa, not all studies agree with one another, for example, Garcin et al. (2007) report drier climate during the LIA (AD 1550-1850).

Kiage and Liu (2009) find that the east African climate has been mostly dry since AD 1650, yet punctuated by centennial to decadal-scale wet and dry episodes, with two dry periods (AD 1650 to AD 1720) coinciding with the LIA. Russell et al. (2009) report that climate between AD 1450 – 1750 was wet in eastern Africa (Verschuren et al., 2000; Stager et al., 2005) but dry in the western rift in Uganda, Tanzania, and Malawi (Russell and Johnson, 2007) with major climatic events occurring about AD 100, 1000, 1250, 1600, and 1800 (Verschuren et al., 2000; Alin and Cohen, 2003; Russell and Johnson, 2008). Bessems et al. (2008) find a period of extreme drought in equatorial East Africa occurring roughly 200 years ago. These examples further demonstrate the potential variability of climate on the African continent. Explaining the regional and temporal differences observed in the different studies is a continuous challenge for researchers.

Perhaps even more difficult to determine are the mechanisms driving the observed climate variability. When viewed on a longer timescale the effects of the Milankovitch cycles on Africa's climate are observable. Orbital precession cycles produce 19- to 23-thousand year fluctuations in insolation resulting in observable climate change in tropical Africa during the Pleistocene (Gasse, 2000; Scholz et al., 2007). A large number of studies report a shift to more stable, humid conditions over a large part of Africa causing significant rises in lake levels, roughly 70 kyr ago, and coinciding with diminished orbital eccentricity and a reduction in extreme climatic events related to precession-dominance (Scholz et al., 2007). Even when examining climate change resulting from orbitally-driven insolation changes many unresolved issues still remain, such as latitudinal gradients, regional patterns, and even the exact timing of climate changes in the tropics in

relation to higher-latitude regions (Gasse, 2000; Trauth et al., 2003; Bessems et al., 2008).

Lately a number of studies trying to identify the cause of smaller scale, decadal to century, climatic changes have found a compelling relationship between solar cycles (flares and minimums) and stratospheric and tropospheric weather systems (Stager et al., 2007 and references therein). Verschuren et al. (2000) found that all three of the severe drought events occurring within the past 700 years coincide with periods of high solar radiation, and that intervening times of increased moisture occurred during periods of low solar radiation, which suggests a relationship between solar radiation levels and decade-scale rainfall variability in this region.

Lake Naivasha had highstands (high lake levels) during each of the last three solar minima (Maunder, Sporer, and Wolf) (Thompson et al., 2002). By studying Lake Victoria during the 20th century a relationship between the 11 yr sunspot cycles and lake level maxima was identified (Stager et al., 2007). The increased lake level was the result of positive rainfall anomalies, which occurred roughly 1 year before the solar maxima. The same relationship was observed in five other lakes in East Africa, suggesting that while the effects of irradiance fluctuations due to sunspot cycles are weak, the effects on tropical rainfall might be amplified due to interactions with sea surface temperature and atmospheric circulation systems (Stager et al., 2007). While there are many studies with evidence in favor of solar forcing impacting climate, many researchers still caution that this relationship and the spatial extent and temporal persistence is not well understood, and that much is yet to be discovered (Johnson et al., 2002; Verschuren, 2004; Russell and Johnson, 2007; Kiage and Liu, 2006; Bessems et al., 2008).

Flora & Fauna

Aside from the wetlands associated with GWD, the lake margins of Eyasi are virtually bare though further away grow short grasslands of *Diplachne fusca* and *Sporobolus spicatus* (Hughes and Hughes, 1992). The trees growing just beyond the lake margin include acacia and palm and much further away baobab can be found. At GWD sites *Cyperus laevigatus*, *Typha*, and sedges (exact species TBD by Barboni) grew, but were restricted to growing close to the GWD (Figure 6 A, B, C, D). Salt was observed as crystals on mud on the edges of sites. Onion is the main crop observed growing within the basin (Figure 6 E).

In the past the basin was home to many of East Africa's native wildlife; however, extensive hunting for food has greatly decreased the populations. In more remote regions, away from human settlements, giraffes, elephants, zebras, gazelles, and dikdik, for example, can still be found. Waterfowl, such as flamingoes, are common when the lake is present and gather in small numbers around GWD sites. Egyptian geese, flamingoes, sacred ibis, marabou stork, egrets, Blacksmith lapwing plovers, and pelicans were all observed at GWD sites while in the field (Figure 7 A, B, C). By far the most common animals in the basin are the herds of livestock (cows, sheep, and goats) raised by the local people (Figure 7 D). It is the herds of domesticated animals that have the largest bioturbation impact on the GWD sites since hippopotamus are rare in this part of the basin.

Hydrology

The main tributary into Lake Eyasi is the Sibiti River, entering the basin from the south, however it only ever flows during very wet years, and like most other water

Figure 6. Photographs of vegetation common to the Eyasi Basin. (**A**) View looking towards Lake Eyasi (note escarpment of northwest margin in background) demonstrating the bare lake margin, GWD site with Typha and sedges visible in lower left corner, and the tops of palm and acacia trees are in the foreground. (**B**) View 180 degrees from image A showing the mix of Acacia and Palm trees growing beyond the lake margin. (**C**) Baobab growing far from the lake. (**D**) View looking down the northeast margin of Lake Eyasi demonstrating the gradation from Acacia/Palm mix to dried grass, and eventually to the bare soil of the lake margin. Note: the pool of water just visible in the foreground is a man-made feature. (**E**) Photograph of core site 1, showing tall stands of Typha and short grass in the foreground. (**F**) One of the many onion farms surrounding the lake. This particular farm utilized GWD to water crops via surface irrigation (note channels in dirt).

Figure 7. Images of wildlife around Lake Eyasi. (**A**) and (**B**) show flocks of birds on the distal reaches of a GWD site. Species present in A include: Marabu stork (tall one in background) and Egyptian geese, in B include: Pelicans, cattle egrets, egyption geese, and one flamingo. (**C**) Egyptian geese flying in front of Eyasi fault escarpment (background) and a flock of flamingoes around what remains of the lake water, lower right corner. (**D**) Local boys moving their livestock, which includes donkey (farthest left), cattle (middle of image), sheep and goats (front of the herd).

sources in this area, the waters of the Sibiti typically evaporate before ever reaching the lake (Hughes and Hughes, 1992). In wet years, fluvial drainage from the Serengeti to the northwest and from the uplifted metamorphic highlands to the southeast also contribute to the lake's input (Deocampo, 2005). The most likely groundwater source for the GWD occurring along the northern margin is the Ngorongoro Volcanic Highlands to the north, while the GWD observed on the southeast margin of the lake is likely sourced from the uplifted metamorphic highlands that run parallel to the lake margin (Figures 3 and 8). Elizabeth Miller at Rutgers University conducted hydrologic modeling of the entire Eyasi Basin, and a general travel time for GW to the site fell within 400-1000 years travel time, depending on the path taken. Elizabeth Miller is conducting continued analysis of GW pathways and travel times at this time.

Remote Sensing

The Landsat program, a joint effort between the USGS and NASA, has produced one of the longest continuous records of natural and human induced changes on the global landscape (USGS, 2012). The first satellite, Landsat 1, was launched in 1972, since then 5 additional satellites have been successfully launched (USGS, 2012). Presently only Landsat 5 and 7 remain operational however there are plans for a new satellite to be launched in early 2013 (USGS, 2012) (Table 1).

All of the Landsat satellites captured images of earth in 185 km wide swaths, moving in a descending orbit (North to South) over Earth's sunlit side (USGS, 2012). The satellites would pass over the same point on earth every 16-18 days, depending on the satellite (USGS, 2012). Landsats 1, 2, and 3 contained a Multispectral Scanner (MSS), producing images with a resolution of 80 m and recording four spectral bands (Table 2) (USGS,

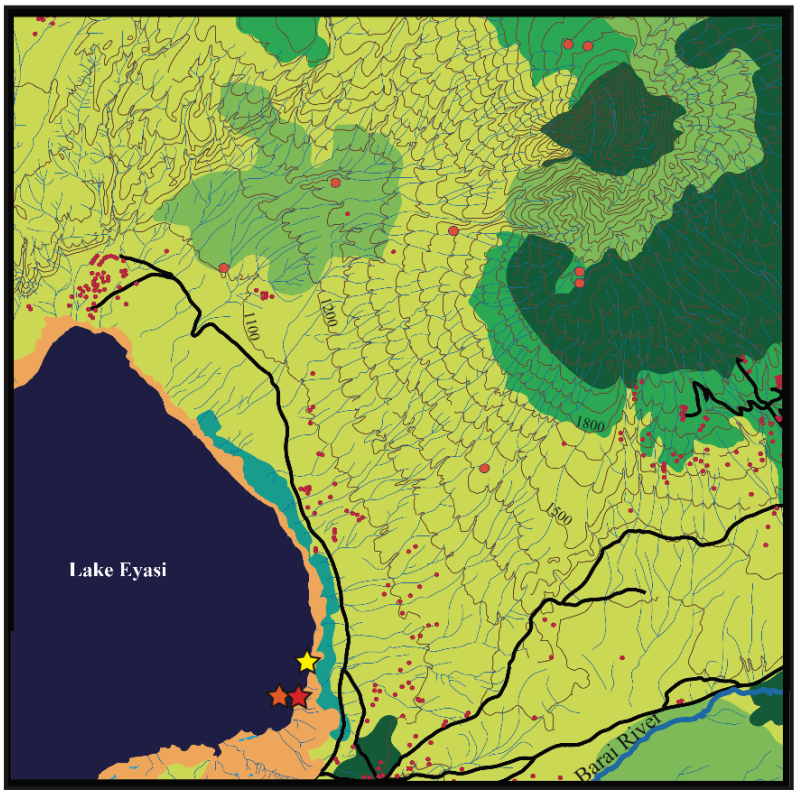

Figure 8. Topographic map, modified from the 1974 topograph published by the Government of the United Republic of Tanzania. Thin blue lines represent water drainage paths however these rarely have water running through them except during wet years. Red star: Core site 1, orange star: Core site 2, yellow star: Core site 3. Contour lines are 100 meter intervals. For original, untraced topographic map refer to appendix 11.

Table 1. Landsat mission dates.

Satellite	Launch Date	Decommission Date	Sensors
Landsat 1	July 23, 1972	January 6, 1978	MSS/RBV[1]
Landsat 2	January 22, 1975	July 27, 1983	MSS/RBV[1]
Landsat 3	March 5, 1978	September 7, 1983	MSS/RBV[1]
Landsat 4	July 16, 1982	June 15, 2001	MSS/TM
Landsat 5	March 1, 1984	Operational	MSS/TM
Landsat 6	October 5, 1993	Did not achieve orbit	ETM[2]
Landsat 7	April 15, 1999	Operational	ETM+[2]
LDCM (Landsat 8)	No earlier than February 11, 2013		OLI/TIRS[3]

[1]Initially, Return Beam Vidicon (RBV) was primary; however, MSS became the primary sensor in time.

[2]Landsat 6 carried the Enhance Thematic Mapper sensor. Landsat 7 carries the Enhanced Thematic Mapper Plus sensor.

[3]LDCM (Landsat 8) will carry the Operational Land Imagery (OLI) and Thermal Infrared Sensor (TIRS)

*Table recreated from USGS (2012).

Table 2. MSS band designations.

Landsats 1,2,3 spectral bands	Landsats 4,5 spectral bands	Wavelength (µm)	Resolution (m)	Use
Band 4 – green	Band 1 – green	0.5-0.6	80	Emphasize sediment-laden water and delineates areas of shallow water
Band 5 - red	Band 2 - red	0.6-0.7	80	Emphasizes cultural features
Band 6 – near IR	Band 3 – near IR	0.7-0.8	80	Emphasizes vegetation boundary between land and water, and landforms
Band 7 – near IR	Band 4 – near IR	0.8-1.1	80	Penetrates atmosphere haze best; emphasizes vegetation, boundary between land and water, and landforms.

*Table recreated from USGS (2012)

2012). Resolution of 80 m means that the side of a single pixel measures 80 m across, thus 1 pixel is 80 m by 80 m.

Landsats 4 and 5 contain the Thematic Mapper (TM) sensors capable of recording several additional bands in the shortwave infrared (SWIR) spectral range, has a resolution of 30 m for visual, SWIR, and near IR bands, and added a 120 m thermal IR band (USGS, 2012). The Enhanced Thematic Mapper Plus (ETM+) lies on board Landsat 7 and boasts 30 m resolution for visible, near IR, and SWIR bands, a 60 m spatial resolution thermal band, and a 15 m panchromatic band (USGS, 2012) (Table 3). In May of 2003 the Scan Line Corrector on board Landsat 7 failed causing gaps in some of the data sets, however this had no affect on the images used in this study (USGS, 2012).

N-alkanes

N-alkanes, the dominant component in epicuticular waxes of plants, are straight-chain hydrocarbons, relatively large and stable structures capable of being well preserved in sediments (Eglinton and Hamilton, 1963; Meyers and Ishiwatari, 1993) (Figure 9). These chains typically have an odd number of carbon atoms, ranging from 17 to 33 carbons in a chain (Meyers, 1997; Castañeda et al., 2007; Russell et al., 2009; Castañeda et al., 2011). N-alkanes originating from terrestrial plants can be transported by either wind or water, though it is not uncommon for wind to be the dominant mode in arid regions (Meyers, 1997; Castañeda et al., 2007; Eglinton and Eglinton, 2008; Russell et al., 2009; Castañeda and Schouten, 2011). When wind transported, n-alkanes are transported on leaf fragments or other materials such as sediment or as aerosols formed by vegetation fires or simple wind abrasion (Castañeda et al., 2007; Eglinton and Eglinton, 2008; Russell et al., 2009; Castañeda et al., 2011). N-alkanes that are

Table 3. TM and ETM+ band designations.

Spectral bands	Wavelength (µm)	Resolution (m)	Use
Band 1 – blue-green	0.45-0.52	30	Bathymetric mapping; distinguishes soil from vegetationl deciduous from coniferous vegetation.
Band 2 – green	0.52-0.61	30	Emphasizes peak vegetation, which is useful for assessing plant vigor.
Band 3 – red	0.63-0.69	30	Emphasizes vegetation slopes
Band 4 – reflected IR	0.76-0.90	30	Emphasizes biomass content and shorelines
Band 5 – reflected IR	1.55-1.75	30	Discriminates moisture content of soil and vegetation; penetrates thin clouds.
Band 6 – thermal	10.40-12.50	120	Useful for thermal mapping and estimated soil moisture
Band 7 – reflected IR	2.08-2.35	30	Useful for mapping hydrothermally altered rocks associated with mineral deposits.
Band 8 – panchromatic (Landsat 7)	0.52-0.90	15	Useful in 'sharpening' multispectral images.

*Table recreated from USGS (2012)

A.

B.

Figure 9. (**A**) Image of a plant with “leaf waxes” scratched into the leaf wax, which is primarily composed of n-alkanes. (**B**) Molecular stucture of an n-alkane with carbon atoms at the points and hydrogen atoms inbetween. Both A and B provided by Isla Castañeda.

transported to the site by wind or water are in addition to those deposited *in situ* by the plants growing in the GWD-fed wetland.

Shorter chains (C_{17}-C_{21}) are typically associated with aquatic plants, while longer chain lengths (C_{25}-C_{33}) are sourced from terrestrial plants (Giger et al., 1980; Cranwell et al., 1987). The distribution of the different chain lengths can be used to provide information on the vegetation types in an area; for example, it is generally agreed that C_{31} n-alkanes are produced mainly by grasses while C_{27} and C_{29} are characteristic of deciduous trees (Giger et al., 1980; Cranwell et al., 1987; Eglinton and Eglinton, 2008). For intermediate chain lengths, such as C_{19}, C_{21}, C_{23}, and so on, sources are less clear, most likely produced by a mix of aquatic and terrestrial plants (Giger et al., 1980; Cranwell et al., 1987; Eglinton and Eglinton, 2008; Castañeda et al., 2011).

In the case of the Eyasi groundwater-fed wetlands it is known that pollen from species farther from the wetland (not in situ) and sediments are wind transported into the system and deposited at the core site (Ashley et al., 2013). Knowing this it can be assumed that some of the n-alkanes (not including those from in situ deposition) are also wind transported to the site as n-alkanes commonly stick to sediments and other wind transported material in addition to being transported directly from the leaf by wind. As a result the n-alkane data likely represents the basin as a whole and not just those plants growing immediately over the site. Additionally the presence of n-alkane with chain lengths commonly formed by grasses and trees also indicates the ability of wind transport as neither grasses nor trees were growing within a few meters of the site yet their signature can be seen in the data.

In addition to using n-alkane chain lengths to determine vegetation type, the carbon isotopic composition of specific n-alkanes can be used to distinguish between the different photosynthetic pathways utilized by plants (O'Leary, 1981; Collister et al., 1994; Castañeda et al., 2007; Castañeda et al., 2009; Castañeda et al., 2011; Castañeda and Schouten, 2011). Trees, shrubs and other temperate species make up the majority of C_3 plants, while grasses and sedges, more drought resistant species, represent the bulk of C_4 plants (Collister et al., 1994; Raven et al., 1999; Castañeda et al., 2007; Castañeda et al., 2009; Castañeda et al., 2011; Castañeda and Schouten, 2011). The carbon isotopic composition of plants utilizing the C_3 photosynthetic pathway tends to average around -36‰, however plants utilizing the C_4 photosynthetic pathway tend to average around -21.5‰ (Cerling et al., 1993; Collister et al., 1994). End-member values, while not varying too much, are reported differently depending on the study. This being said, most studies will look at the specific values for plants within the study region to better understand the isotopic end-member values specific to the C_3 and C_4 plants in the region. To better constrain the results found here it would be best to determine the specific isotopic composition of the different C_3 and C_4 species in the immediate area around the core site and basin area at large, unfortunately this was beyond the scope of this study.

METHODS

Remote Sensing

Landsat imagery of Lake Eyasi was acquired from the USGS website, (http://earthexplorer.usgs.gov/). Imagery for this analysis was limited to what was available on the site as well as cloud free imagery (Appendix 2). Landsat satellites do not

have the capability to measure spectral bands unaffected by cloud cover as some satellites do. It is possible to use imagery with some cloud cover if they did not cover the cropped region, otherwise the presence of clouds would skew the analysis. The software used to manipulate and analyze the Landsat imagery was ERDAS Imagine 9.0. Due to time constraints, and in order to increase the number of usable images, all images were cropped so only the northeast corner, and future field site, of Lake Eyasi was studied.

The methods of image analysis that were used are outlined by Ozesmi and Bauer (2002) and have been used to locate and monitor wetlands previously. A normalized difference vegetation index, NDVI, was applied to the cropped images. The NDVI ratios the near infa-red band with a visual band, in this case the band for the color green. The resulting image shows areas of higher amounts of vegetation in warmer colors (yellow, orange, red with red representing the highest amounts) and the areas with cooler colors (greens, blues, etc.) as having less vegetation. This analysis was performed on as many images as possible with the exception of those with too much cloud cover over the site. The remote sensing analysis portion of the project was conducted at the Center for Remote Sensing and Spatial Analysis (CRSSA) at Rutgers University under the guidance of Director Dr. Richard Lathrop.

GoogleEarth was used to augment the Landsat study as the majority of GoogleEarth imagery is at a higher resolution, now less than two meter resolution for the newest imagery, than Landsat imagery and, like the Landsat data, is available free of charge. When ground-truthing (physically visiting a site while in the field) was not feasible, GoogleEarth imagery could be used as a means for visually verifying results. Additionally, after the field season, a large portion of the lake margin imagery was

updated to sub-two meter resolution allowing for additional identification of numerous smaller GWD features around the northeast and southeast lake margin.

Field Methods

Site Description

Observations were made and photographs taken of the physical setting and GPS locations recorded for the GWD sites visited, in particular those from which cores were taken (Table 4). Water samples were collected at each GWD site, and in situ measurements of water temperature and pH taken (Ashley, unpublished data). Samples of vegetation surrounding and supported by the GWD were taken, along with photos, and soil samples (Barboni, unpublished data).

Core Collection

A total of 7 short cores were collected from 3 different GWD sites using a Livingstone piston corer (Appendix 3). At each location the site for coring was selected as far into the wetland as possible in areas of minimal "large animal" bioturbation. Standard coring procedures were followed (Wright, 1967).

The Livingstone corer was assembled in the field at each coring location. Once chosen the site was carefully cleared of large plants, at the same time the halves of the core liner were labeled with location, date, up direction, and core number. The corer was positioned vertically over the core site and kept as vertical as possible throughout the coring process. The corer was then pushed straight down into the wetland until it was not possible to push any further. The corer was then lifted straight out and carried vertically to a dry flat location for core extraction.

Table 4. GPS locations for coring sites.

Site Name	Latitude	Longitude	Notes
Core Site 1: Kisima Ngeda-Barazanee	3°29.141'S	35°20.892'E	Few meters walk from core site 2
Core Site 2: Kisima Ngeda-Kidogo	3°29.105'S	35°20.586'E	"blister" wetland
Core Site 3: Kisima Ngeda	3°28.572'S	35°20.945'E	Site closest to tented camp

Cores were extruded onto one half of butyrate tubing, which were split prior to leaving for the field, the other half then placed on top and the two taped together. Next the core was plastic-wrapped; plastic end caps labeled with core site, date, and top/bottom designation were applied to both ends and taped into place. Once collected, cores were stored horizontally, and with no refrigeration available in the field, care was taken to keep cores out of direct sunlight, in as cool a location as possible. Numerous attempts were made to take multiple cores from the same coring hole however after initial core removal the holes filled back in and secondary core retrieval was determined to be impossible (Figure 10).

Lab Methods

Sedimentology

Initial Description

The cores were analyzed at LacCore, Limnological Research Center Core Facility, University of Minnesota - Minneapolis campus, using this lab's standard initial core description (ICD) procedures, which included: whole core multisensory logging, core splitting into work and archive halves, core surface preparation, digital whole core imaging (Appendix 3), ICD sheet production, split core multisensory logging, macroscopic sediment description, microscopic sediment description (smear slides), cold storage in D-tubes, and data archiving. Prior to splitting, cores were run on a Geotek Multisensor Core Logger (MSCL), which measured sediment density, acoustic wave velocity, electrical resistivity, and loop-sensor magnetic susceptibility at a 0.5 cm resolution. It should be noted that it was not possible to calibrate the Geotek Multisensor Core Logger (MSCL) to the core liner used, so the results from this machine can only be

Figure 10. **Upper image**: field assistants pushing corer into the ground to collect Core 1A. **Lower image**: Core 1A has been extruded and encased in core liner and is being wrapped and secured for transport.

viewed in relative and not absolute terms.

Each core was then split, scraped, and working halves imaged on a digital line scanner at 10 pixels per millimeter (~300 dpi) resolution. The archived halves were labeled, wrapped in plastic wrap, and stored in a cold storage unit at a maximum of 13^{o}C (55 ^{o}F). Both the cores and the images were used when describing the cores. A Munsell Color Chart was consulted when determining the colors of the cores. Smear slides were collected at regular intervals and examined under microscope to aid in the physical core description. A Geotek XYZ core scanner was used to collected high-resolution (0.5 cm) point-sensor magnetic susceptibility. When not in use or during the overnight periods the working halves were rewrapped in plastic wrap and stored with the archived halves in cold storage. Working and archived halves were returned to Rutgers University for storage and future work.

Sub-sampling

Sub-sampling of the core was done at Rutgers University. Each core was cut into 1 cm thick sections that were then further divided based on the amount or volume of sample needed for each analysis (Figure 11). Due to the limited amount of core collected each 1 cm slice was subdivided and no excess remained. When evident, material pushed down during the coring process was identified and removed.

Percent Sand

Methods were adopted from Folk (1980) and Lewis and McConchie (1994). Grain size was measured for every other centimeter in Core 1A. The small amount of core material meant that it was not possible to perform a full grain size analysis; fortunately it

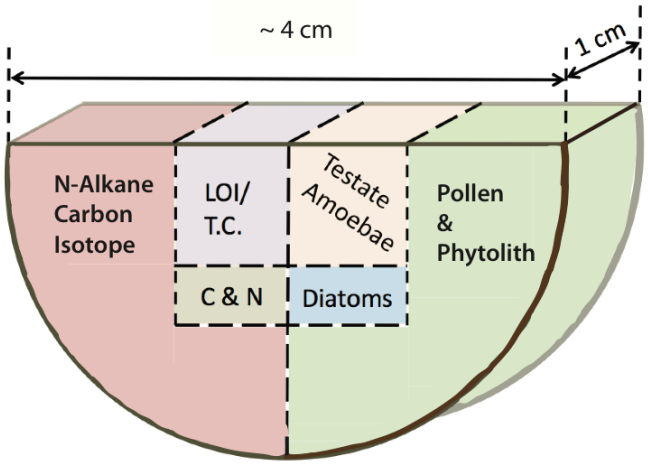

Figure 11. Diagram of a 1 cm thick core slice for sub-sampling. When possible sub-samples were collected from the same location in the core slice as demonstrated with the dashed lines. LOI/T.C. (purple) - 1 cm3, Testate Amoebae (orange) - 1 cm3, carbon and nitrogen (C&N) elemental/isotopic analysis (tan) - ~10 mg, diatoms (blue) - ~10 mg, N-alkane carbon isotope (red) - >/= 5 g, pollen and phytolith (green) - >/= 5 g. When necessary material pushed down during the coring process, found around the rim of the core slice, was removed, weighed, and stored.

was possible to characterize the larger fraction, greater than 63 microns. Samples were collected at a known volume of one cubic centimeter. Each 1 cm^3 sub-sample was dried over night at 105 ^oC and dry weight recorded. Samples were then soaked in distilled water and agitated with steel spatula to break apart clumps of organic and clay material. The muddy mixture was then wet sieved through a 63 micron mesh screen. All material greater than 63 microns was then dried over night (at 105 ^oC). Once dried organic material was then removed and the remaining sediment fraction weighed to determine the weight percent of material larger than 63 microns, which represents the fraction equal to or larger than fine sand.

Sedimentation Rate

Taking the amount of core material above the level of the age date and dividing by the maximum and minimum age determined by the radiocarbon dating provided basic sedimentation rate for the upper interval of the core only. This sedimentation rate was then compared to similar studies in the area to see reasonability.

Geochemical Analysis

Sequential Loss On Ignition

The procedure used for sequential loss on ignition follows Folk (1980) with some adjustments based on the research presented in Heiri et al. (2001). LOI was measured for every other centimeter of Core 1A. Each sample was air-dried overnight, then homogenized with mortar and pestle and dried again over night at 105 ^oC and dry weight recorded. The dried sample was then transferred to a cleaned and dried crucible and the combined dry weight of both recorded. Crucible and sample where then heated in a furnace for 4 hours at 550 ^oC, 4 hours as opposed to the standard 2 hours was chosen due

to the high amount of organic matter in the sample (Heiri et al., 2001). The furnace used was a Barnstead: Thermolyne furnace, model series FB1400. After four hours samples were cooled to room temperature and the weight recorded. The percent of sample weight lost equals the amount of organic carbon in the sample.

Next the samples were returned to the furnace for an additional two hours of heating at 990^{o}C. After the samples were again allowed to cool to room temperature they were reweighed. This time the percent weight lost when multiplied by a constant 1.36 provides the weight of carbonate content in the sample. Combining the two calculated weights gives the total amount of carbon in the sample.

Total Organic Carbon and Total Nitrogen Bulk Elemental & Isotopic Analysis

Sub-samples were run at the University of Massachusetts – Amherst under the guidance of Dr. Finkelstein. Total organic carbon, total nitrogen and stable isotopes for both was measured for every centimeter of Core 1A. Sub-samples for carbon and nitrogen analysis were collected, dried overnight at 150 ^{o}C, and homogenized using mortar and pestle. A small portion of each powdered sample (between 2 and 25 mg) was decalcified with HCl (1 N; 30 ml) for determination of the organic carbon (C_{org}) and nitrogen (N) content of the samples. C_{org}, N, d^{13}Corg and d^{15}N values were determined using a Costech Elemental Analyzer connected on-line to a ThermoFinnigan Delta V mass-spectrometer. Powdered and weighed sediment samples placed within silver capsules were inserted in the autosampler of the elemental analyzer and combusted. The d^{13}C composition of the resulting CO_2 gas was calibrated against an internal laboratory standard (acetanilide, d^{13}Corg=-29.85‰), expressed relative to the Vienna Peedee

Belemnite (VPDB) international standard. The $d^{15}N$ values are also calibrated against an internal laboratory standard (acetanilide, $d^{15}N$=-0.26x), expressed relative to air.

N-alkane Isotopic Analysis

In order to have enough material to be able to run this analysis, 4 centimeters of sediment had to be combined into one sample. So starting from the top, every 4 centimeters were combined and run as one sample. Clayton Magill at Penn State University performed the n-alkane specific carbon isotope study (Appendix 4).

Biological Analysis

Seed Picking

Seeds were collected from the base of the upper interval of the archived half (between 28 and 29 cm depth). The material from the core was placed in deionized water, gently agitated to break apart, and slowly looked through for seeds with the aid of a microscope. Once collected the seeds were sent to Beta Analytic for analysis.

Diatoms

R. Bernhart Owen carried out diatom preparation at his lab in Hong Kong Baptist University. Methods were reported as follows. Carbonates were removed by adding HCl followed by rinsing with distilled water, which assisted with disaggregation. Samples were then dried on smear slides and mounted using naphrax. A minimum of 300 diatoms were counted along transects on each slide. Taxa were identified to species level using light microscopy with phase contrast at 1000×, with reference mainly to the works of Gasse (1980, 1986). Several diatom identifications were confirmed using a Leo 1530 Field Emission Scanning Electron Microscope.

Testate Amoebae

Sub-samples for the testate amoebae analysis were collected at a known volume of one cubic centimeter. The procedure used followed those of Charman (2001). The weight was recorded, sample placed in a beaker, and approximately 100 ml of distilled water added. Sample was then gently broken apart and the slurry heated to a boil for 10 minutes, periodically stirring to help further disaggregate the sample. After ten minutes the sample was washed through a course sieve (300 micron). Care being taken to always use deionized water. The portion caught in the sieve was saved for later use in seed picking. The rest of the sample (<300 microns) was then back sieved through a fine sieve (10 microns). The material caught by the fine sieve, material less than 300 microns but greater than 10, was transferred to a separate test tube for testate amoebae analysis. The remaining sample (<10 microns) was saved to check for the absence of testate amoebae, once tested this portion of the sample was discarded. Due to time constraints testate amoebae were examined every 5 centimeters down core. For each sample five drops were examined for the presence or absence of testate amoebae.

Radiocarbon Dating

Refer to the following link from Beta Analytic's website, detailing the methodology used for AMS radiocarbon dating: http://www.radiocarbon.com/PDF/Beta-AMS-Methodology.pdf

RESULTS

Remote Sensing

Through the NDVI (Normalized Difference Vegetation Index) analysis it was possible to identify regions of the Lake Eyasi margin that remained consistently highly vegetated over many years. When the northeast corner of Lake Eyasi was examined four potential GWD features were large enough to be captured with the 30 m resolution of Landsat imagery. Each of the four sites was visible in every image analyzed despite varying seasons and droughts (Figure 12). Given the coarse resolution of the Landsat imagery and the relatively small size of the majority of GWD features it is not surprising that Landsat was only able to identify four in this small corner of the lake margin.

A large portion of Eyasi basin was updated to the new GoogleEarth imagery boasting resolution of less than two meters, which made it possible to visually identify 640 additional GWD features along the southeast and northeast margin (Figure 13). At a resolution less than two meters it is possible to distinguish individual trees. Unfortunately, the only portion of the basin not yet updated is the northeast margin of the lake, the field/coring site, where imagery remains too coarse to identify most of the GWD sites along this part of the lake margin.

Sedimentology

Core Description

The core is divided into two distinct layers, a lower interval from 43 cm to 30 cm and an upper interval from 30 to 0 cm. The lower interval was a dark grey color, 5Y 4/1 Munsell, and did not contain any visible pieces of vegetation but contained sediment of

sand, silt, and clay size. Smear slide analysis confirmed the presence of increased clay and the presence fragmented of diatoms. The contact between the upper and lower intervals is not perfectly horizontal, possibly due to the coring procedures (Figure 14). Through visual analysis of Core 1A and core photograph it was determined that the upper interval of the core was black in color, 10YR 2/1 Munsell (Figure 14). The upper interval extends from 30 cm to 0 cm depth and contained large pieces of vegetation throughout with little sediment visible. When analyzed under a microscope, smear slides taken throughout this interval showed numerous diatoms.

Density

As a result of the geotek core scanner not being calibrated to the core liner the results of the density scan can only be considered in relative and not absolute terms. A difference in density between the lower and upper interval of each core was observed, with the lower portions always exhibiting higher densities (Appendix 5). In Core 1A there is an obvious decrease in density between the lower and upper intervals, at roughly 29 to 30 cm depth. Within the upper interval of the core, there is an interval of relatively constant density from 29-20 cm depth, above this point the density continues to decrease steadily up core. Between 10 and 8 cm depth there is a sudden drop in density, this anomaly is due to a small gap in the core and not due to changes in the core composition (Figure 15).

Magnetic Susceptibility

The magnetic susceptibility plots for the 7 cores collected were highly variable. In general regions of high organic matter (OM) had lower susceptibility then those regions that appeared to have higher amounts of sediment, i.e. the lower portions of the

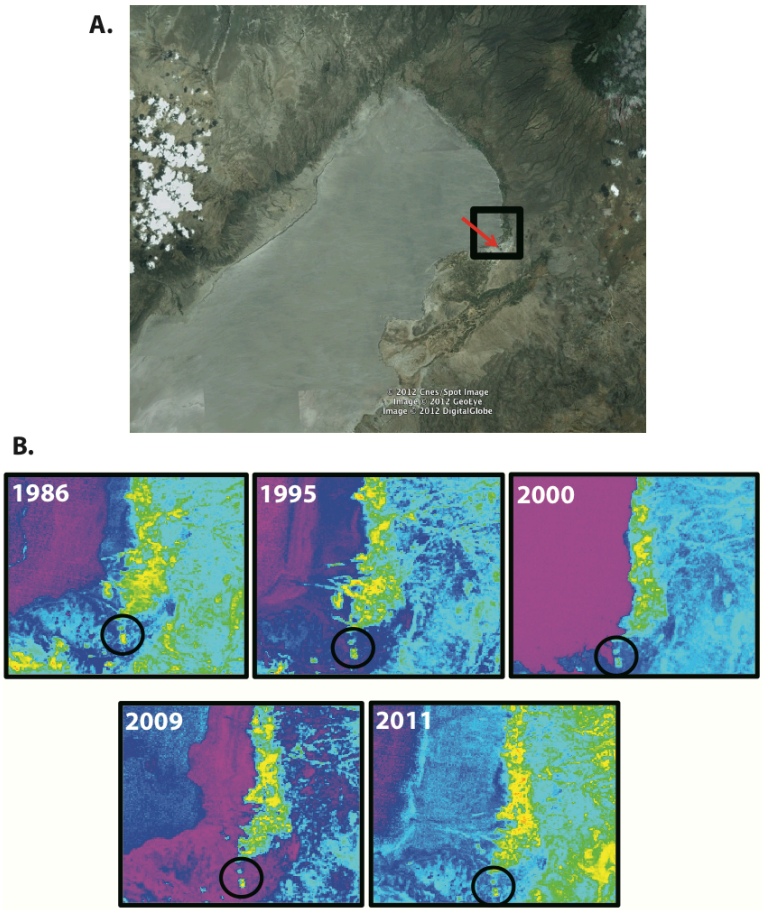

Figure 12. (**A**) Image of the upper portion of Lake Eyasi, from Google Earth, with the focus of the NDVI study outlines in black and a red arrow pointing to the feature circled in B. (**B**) Example of the results from the NDVI study. Warmer colors, such as reds, yellows, or light greens, represent areas with higher amounts of vegetation relative to the rest of the image. Cooler colors, such as blues or purples, represent areas with lower amounts of vegetation relative to the rest of the image. The color scheme represents a continuum with red being most vegetated and purple being least. Note: amount of vegetation is relative to a single image, a color in one image does not mean the same amount of vegetation in another. The black circle highlights two of the suspected GWD features found throughout the course of this study.

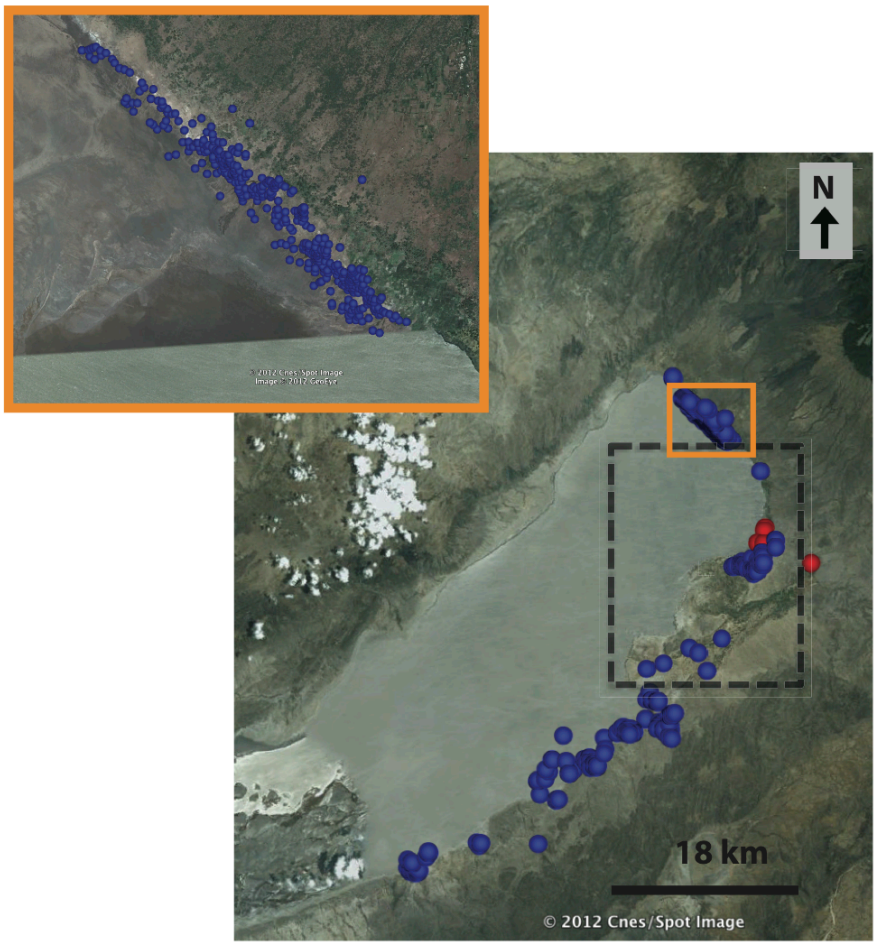

Figure 13. Google Earth image showing location of GWD sites (blue and red dots) along the margin of Lake Eyasi. Blue dots represent GWD sites identified through visual analysis of Google Earth alone. Red dots are GWD sites visited during the field season. The dashed box delineates a region on the Eyasi margin not yet updated to the newest and highest resolution imagery on Google Earth, the rest of the lake margin was covered by the new (<2 m resolution) imagery. The orange box shows the area in the inset image, demonstrating the high volume of GWD sites, in the larger image the dots overlap, making it impossible to see the real number of GWD sites identified. Inset image ~5 km across.

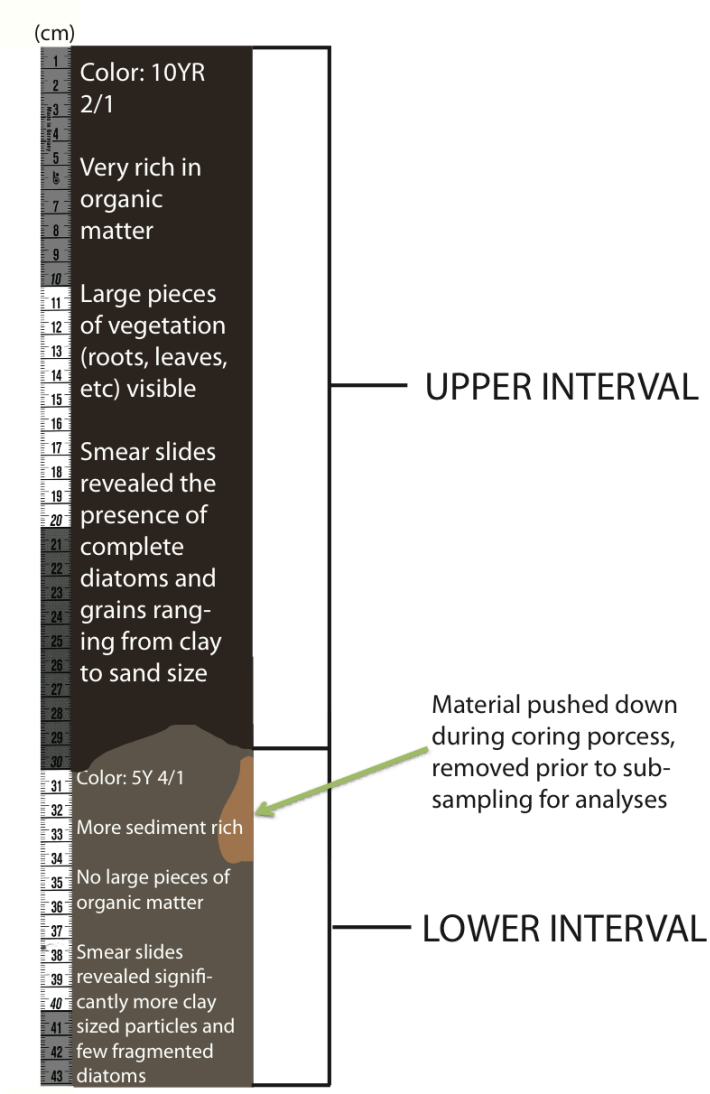

Figure 14. Basic core description for Core 1A. It should be noted that the colors are based on examining the actual core itself and not the photographs, in which the colors appear much lighter. The core was 4 cm across and is drawn here wider to allow for more room for notes. The scale bar on the left is in centimeters.

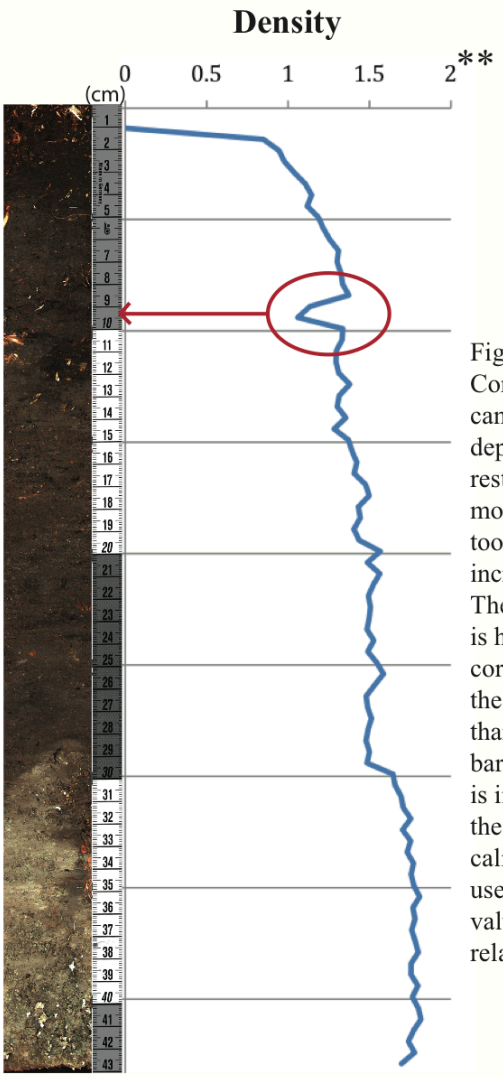

Figure 15. Plot of density down Core 1A. An increase in density can be seen starting at 30 cm depth and continuing for the rest of the core. The very top most 1 cm of core was too loose too register, hence the sudden increase starting at 1 cm depth. The circled portion of the graph is highlighting a region of the core that had a crack causing the density to register lower than had no gap existed. Scale bar is in centimeters. **Note: it is important to remember that the machine was not able to be calibrated to the core liners used, as a result the density values can only be viewed in relative and not absolute terms.

cores. Two of the cores (Cores 2A and 2B) were recovered from a "blister wetland" sourced by GWD. This feature occurred further out on the lake bed, and one core, core 2A, contains considerably more lake margin material than others, and as a result has a significantly higher magnetic susceptibility plot, note the difference in scale (Appendix 6).

Within Core 1A the magnetic susceptibility scan showed a highly variable trend. The lower portion of the core, 43-30 cm, has a slightly higher magnetic susceptibility average of 11.7 SI (x10^-6) (SI = International System of Units) with a standard deviation of 2.26. The average for the upper interval is approximately 8 SI (x10^-6). Within the upper interval from 30-16 cm magnetic susceptibility averages 9 SI (x10^-6) with a standard deviation of 1.76 SI (x10^-6), from 15-5 cm 7.8 SI (x10^-6) with a standard deviation of 1.19 SI (x10^-6), and an average of 2.7 SI (x10^-6) with a standard deviation of 2.79 SI (x10^-6) for the top 5 cm (Figure 16).

Percent Sand

The lower interval of the core from 43-30 cm contained an average of 20% material larger than 63 micrometers (>/= fine sand size) with a standard deviation of 6.37 % greater than 63 μm, 29-16 cm averaged 25% greater than 63 μm with a standard deviation of 6.06% greater than 63 μm, and the top from 16-0 cm averaged 3.2% greater than 63 μm with a standard deviation of 1.73% greater than 63 μm. Averaged weight percent of grains larger than 63 microns showed a decrease in larger grains for the top 14 cm of core (Figure 17).

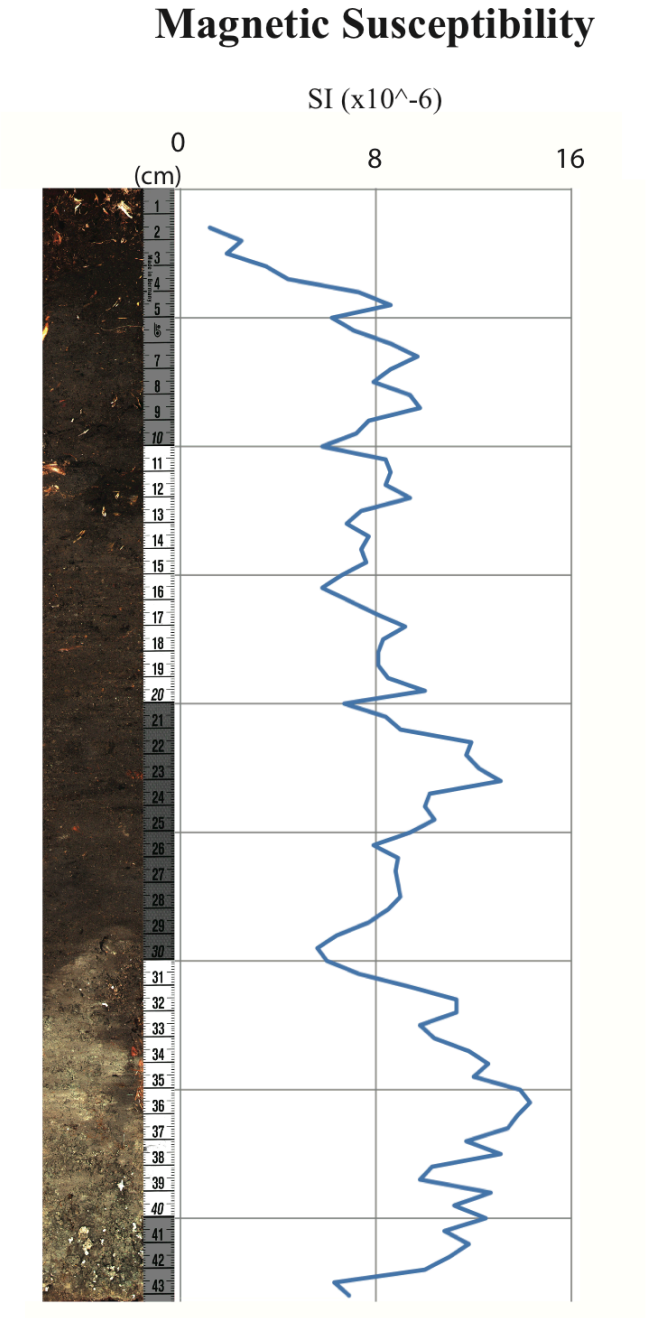

Figure 16. Plot of magnetic susceptability data for Core 1A. For the plots from all the cores see appendix 6. Y-axis is depth in centimeters.

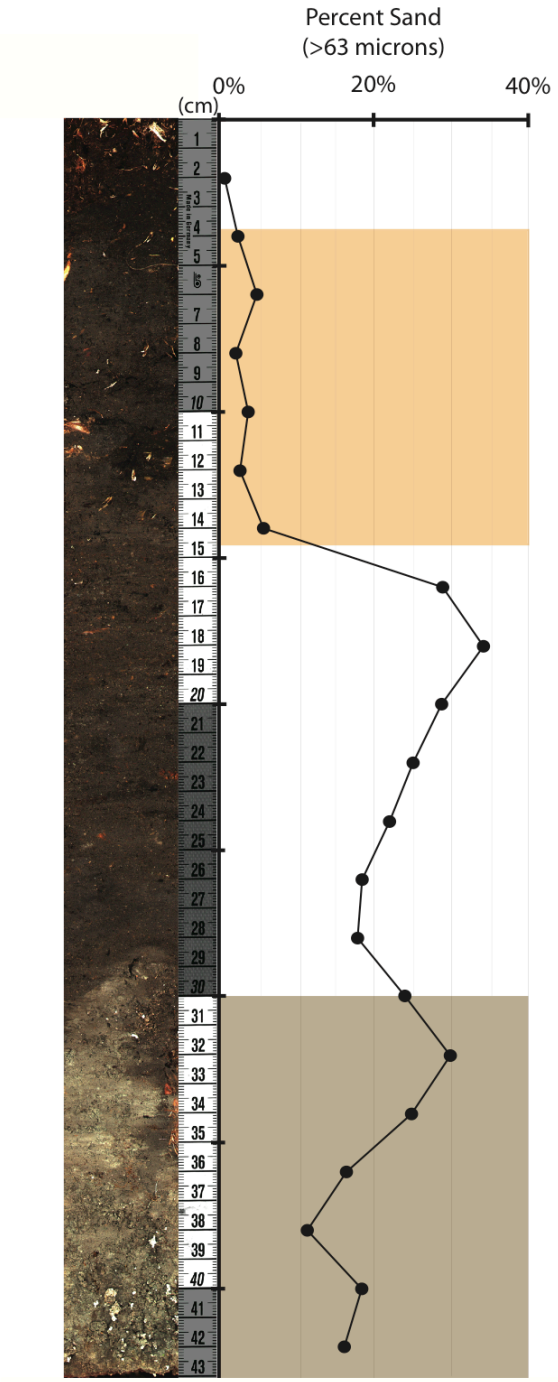

Figure 17. Plot of data points for the percent sand study of Core 1A. Orange shading represents the diatom zone indicating increased salinity in the upper interval of the core. The grey shading indicates the lower interval of the core. Y-axis is depth in centimeters

Sedimentation Rate

Calculated sedimentation rates for the upper interval of the core only ranged from 1.3 mm/yr using the youngest age date reported by the radiocarbon dating (215 years before 2012) to 0.56 mm/yr using the oldest reported age date (497 years before 2012). Sedimentation rates of ~1mm/yr have been reported for other GW-fed wetlands studied in this region (Ashley et al. 2004), suggesting the rates calculated here are reasonable.

Geochemical Analysis

Sequential Loss on Ignition

Overall LOI increased up core with a maximum value of 38.1% organic matter (OM) occurring at 1 cm depth and a minimum of 5.35% OM at 35 cm depth (Figure 18). The lower interval of the core (43-30 cm) had an average LOI of 5.73% OM with a standard deviation of 0.27% OM. Within the upper interval from 29-16 cm averaged 8.72% OM with a standard deviation of 1.22% OM, from 16-5 cm averaged 14.33% OM with a standard deviation of 2.51% OM, and the upper most interval from 4-0 cm averaged 31.98% OM with a standard deviation of 8.77% OM. Due to a malfunction in the furnace used, the second stage of the sequential LOI study to determine percent carbonate was not completed. Those samples run prior to the identification of the malfunction were proven to be inaccurate. There was not enough core material remaining to repeat the analysis, as a result this test was dropped from the study.

Total Organic Carbon – Elemental Analyzer

The lower interval of the core, 43-31 cm depth, averaged 0.88% carbon with a standard deviation of 0.36% carbon. In the upper portion percent carbon averaged

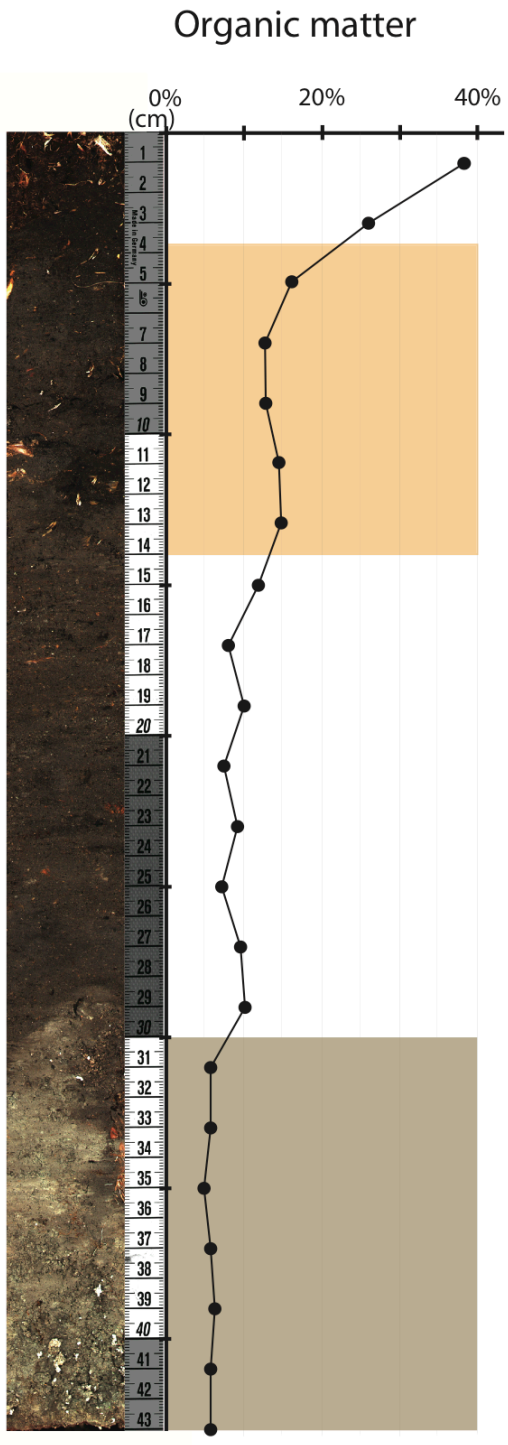

Figure 18. Plot of data points for the first stage of the sequential loss on ignition study of Core 1A. Samples were heated at 550 degrees C for 4 hours, during which time all of the organic matter would burn off. Y-axis is depth in centimeters and lines up with the core image and ruler on the left.

3.55% carbon from 30-16 cm depth with a standard deviation of 0.78% carbon, 7.06% carbon from 15-4 cm with a standard deviation of 2.20% carbon, and 23.67% carbon for the top three centimeters (3-0 cm) with a standard deviation of 3.24% carbon. The maximum percent carbon of 26.85% carbon occurred at 1 cm depth and the minimum of 0.54% carbon occurred at 41 cm depth (Figure 19).

Total Nitrogen – Elemental Analyzer

The lower interval of the core, 43-31 cm depth, averaged 0.06% nitrogen with a standard deviation of 0.023% nitrogen. Within the upper portion percent nitrogen averaged 0.23% nitrogen for 30-16 cm with a standard deviation of 0.053% nitrogen, 0.54% nitrogen for 15-4 cm with a standard deviation of 0.12% nitrogen, and 1.28% nitrogen for 3-0 cm with a standard deviation of 0.14% nitrogen. The maximum percent nitrogen of 1.43% nitrogen occurred at 1 cm depth and the minimum of 0.04% nitrogen occurred at 41 and 43 cm depths (Figure 19).

TOC/TN ratio

C/N ratios, in this case TOC/TN specifically, were calculated for each centimeter of Core 1A. C/N values ranged from 19.2 at 2 cm depth to 11.59 at 11 cm depth. For the lower interval of the core, 43-31 cm depth, C/N averaged 13.85 with a standard deviation of 0.65. Within the upper interval C/N averaged 15.55 for 30-16 cm with a standard deviation of 0.75, 12.76 for 15-5 cm with a standard deviation of 1.06, and 17.61 for the uppermost four centimeters with a standard deviation of 1.86 (Figure 20).

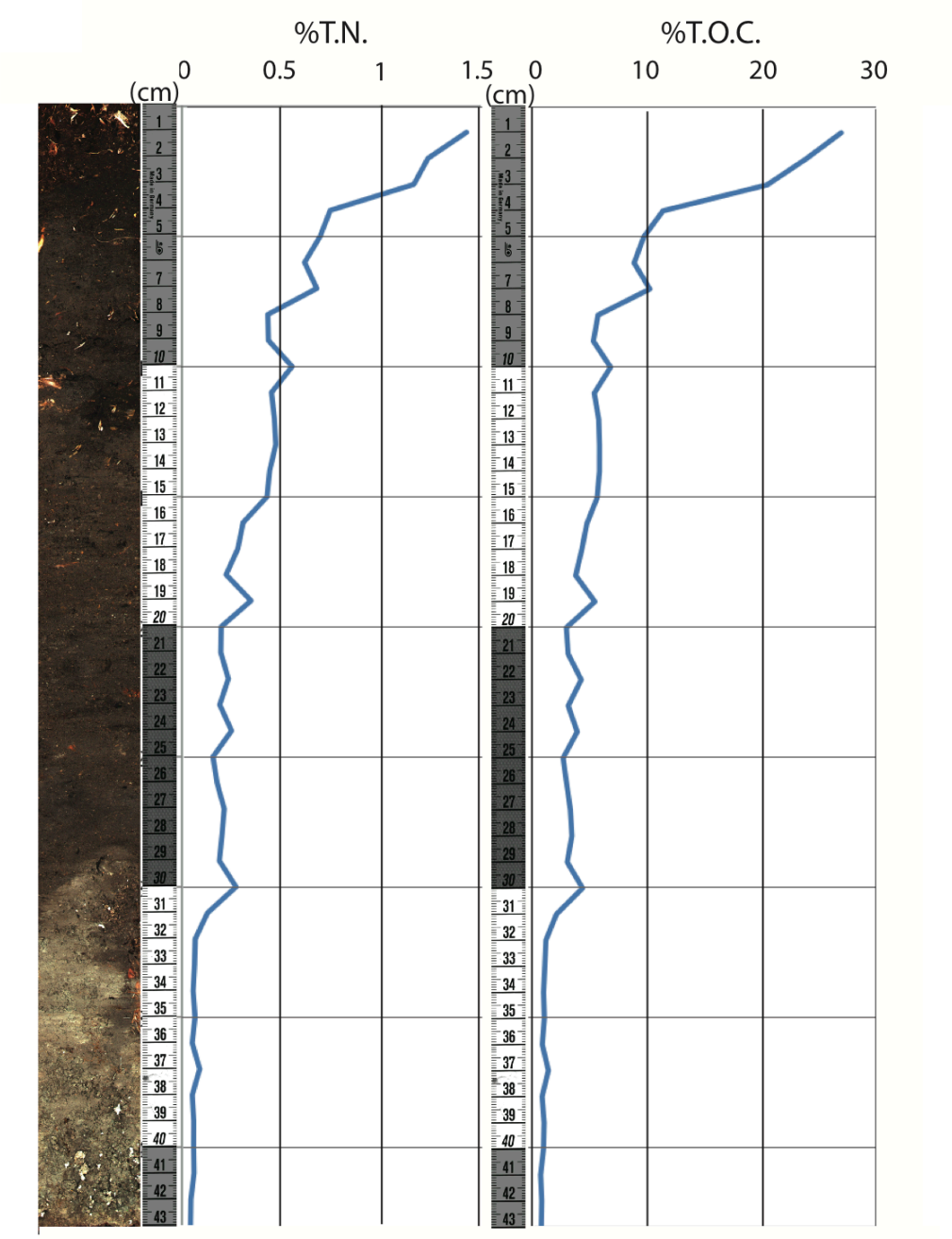

Figure 19. Plot of the total nitrogen (%T.N.) and total organic carbon (%T.O.C.) for Core 1A. Y-axis is depth in centimeters.

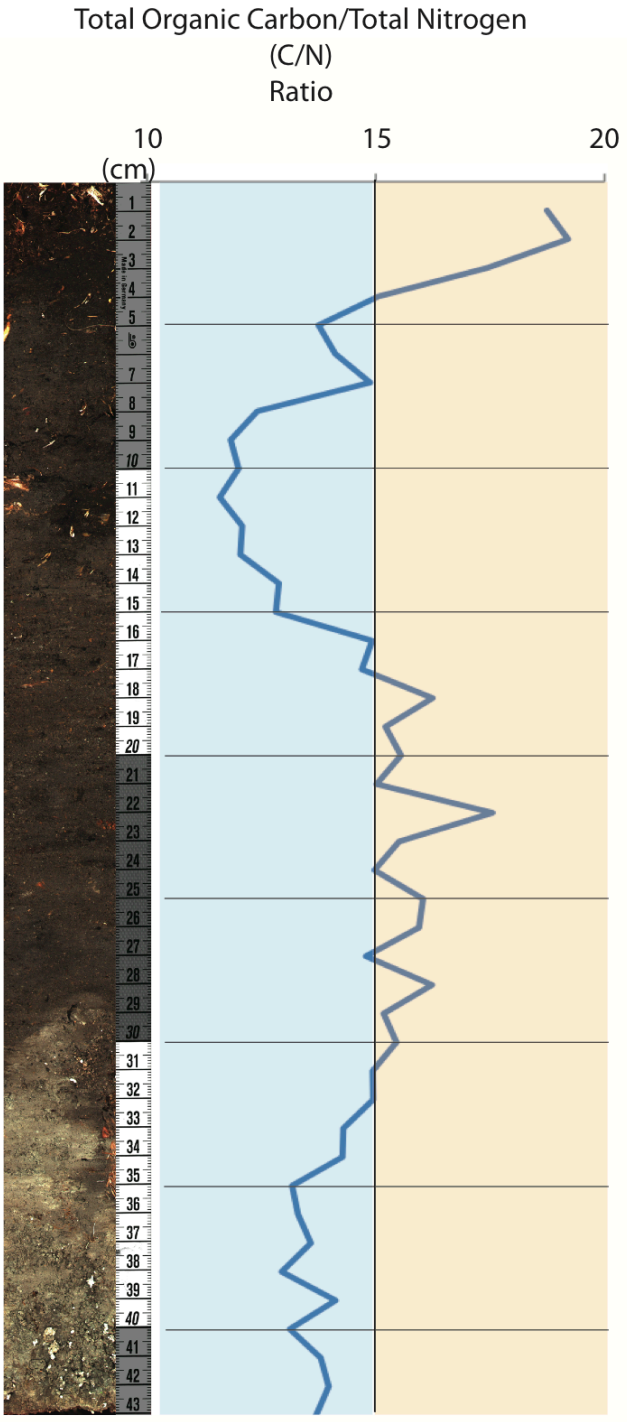

Figure 20. Plot of the total organic carbon versus total nitrogen ratio for Core 1A. Typically a ratio less than 10 indicated an aquatic source for organic matter, and a ratio greater than 20 indicates a terrestrial source. Because wetlands can contain both aquatic and terrestrial case, it is logical that there is a mixed signal. The blue region represents ratios less than 15, suggesting a greater imput from aquatic sources, while the orange area contains ratios greater than 15 suggesting increased input from terrestrial plants. Y-axis is depth in centimeters.

Carbon Stable Isotopes

The carbon stable isotope study compared 13C/12C. The overall average for the core was -22.60 with a standard deviation of 0.71. The average for the lower interval of the core, 43-30 cm, was -22.68 with a standard deviation of 0.467, and the upper interval from 30-15 cm averaged -22.65 with a standard deviation of 0.435, from 14-5 cm averaged -22.95 with a standard deviation of 0.698. The only section of the core showing much variation was the upper 4 centimeters, which averaged -21.20 with a standard deviation of 0.88. The most enriched value of -20.60 occurred at 1 cm depth, and the most depleted value of -23.76 occurred at 14 cm depth. The average standard deviation for those samples ran in triplicate was 0.15 (Figure 21).

Nitrogen Stable Isotopes

The nitrogen stable isotope study compared 15N/14N. The overall average for the core was 2.66 with a standard deviation of 0.496. The lower portion of the core from 43-31 cm averaged 2.39 with a standard deviation of 0.56, while in the upper portion averaged 2.54 for 30-17 cm with a standard deviation of 0.233, 3.16 for 16-5 cm with a standard deviation of 0.184, and 2.26 for 4-0 cm with a standard deviation of 0.291. The most enriched value of 3.44 occurred at 12 cm and the most depleted value of 1.08 occurred at 36 cm (Figure 21).

N-alkane Specific Carbon Isotope data

The n-alkane specific carbon stable isotope study compared 13C/12C in different chain length n-alkanes. For C_{23} the isotopic values range from -16.7 to -21.3, for C_{25} values range from -22.4 to -26.4, for C_{27} values range from -25.7 to -28.0, for C_{29} values

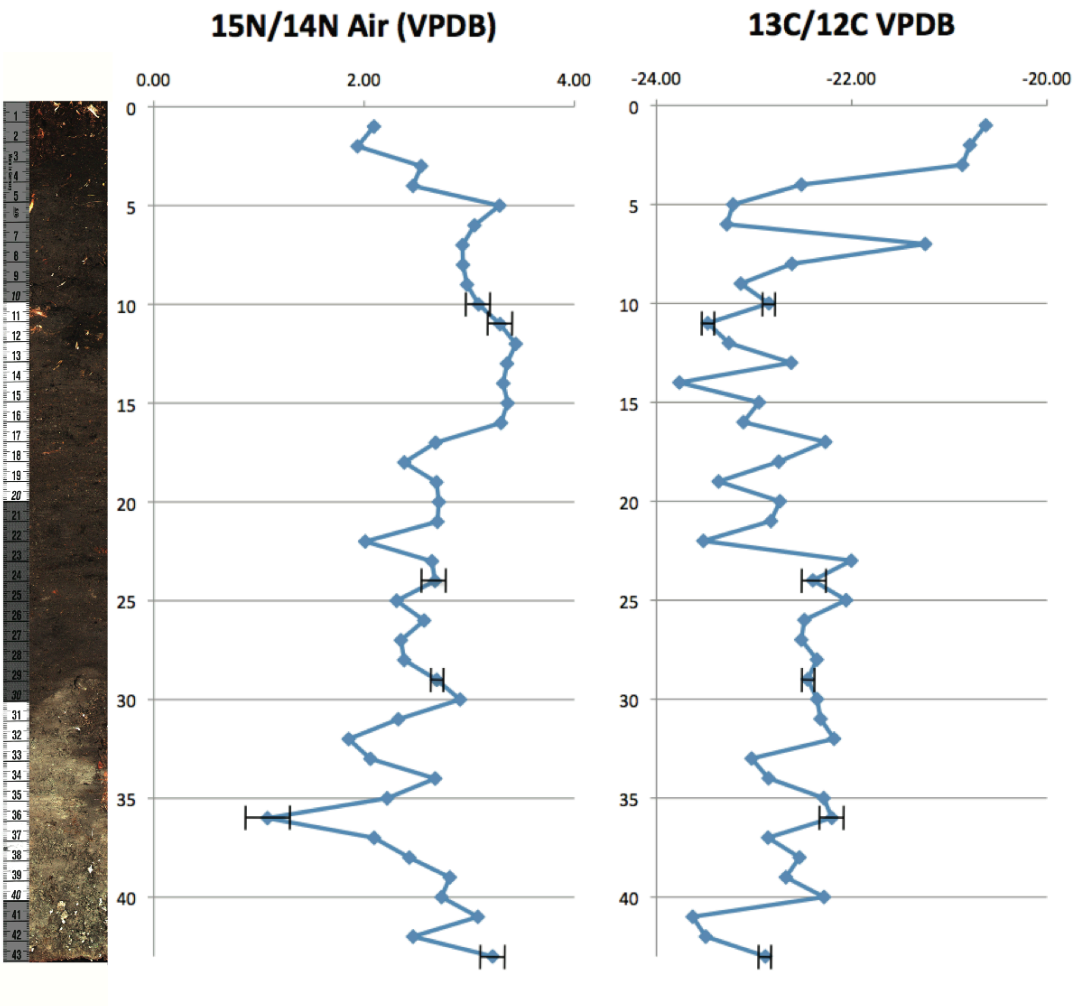

Figure 21. Plot of the nitrogen (left) and carbon (right) stable isotope data for Core 1A. For those samples that were run in triplicate, standard deviation bars were added. The Y-axis is depth in centimeters.

range from -23.7 to -30.7, for C_{31} values range from -22.2 to -25.5, and for C_{33} values range from -22.5 to -25.5 (Figure 22; Appendix 7).

Biological Analysis

Diatoms

R. Bernhart Owen at the Hong Kong Baptist University completed the diatom analysis and interpretation. Five distinct zones were identified based on the condition and species of diatoms observed (Figure 23). The following results were reported:

Zone I (43-39 cm depth) contains infrequent, fragmented diatoms only, with diatoms more common in Zone II (39-29 cm depth), but highly fragmented. Zone III (29-14 cm depth) is characterised by the presence of *Staurosira venter* and relatively abundant *Nitzschia amphibia*. Fragmentation is common, but there are many intact diatoms. *S. venter* and *N. amphibia* occur in fresh to brackish water. Highly saline taxa are scarce, but present. *S. venter* disappears in Zone IV (14-5 cm depth) and *N. amphibia* declines, being replaced by *Rhopalodia gibberula* with an increase in *Caloneis bacillum* and saline taxa (notably *Anomoeoneis sphaerophora*). *R. gibberula* is widespread in lakes and rivers and hot springs, and is often epiphytic. In Africa, it is tolerant of meso- to hyperhaline conditions and is often associated with alkaline lakes. Zone V (5-0 cm depth) resembles Zone III, but with increased *Staurosira*. The saline taxon *A. sphaerophora* also occurs.

Testate Amoebae

Testate amoebae were not found in the lower interval of the core (43-30 cm depth) and in very low numbers (<10 specimen per drop) throughout the upper interval of the core (29-0 cm depth). Due to the relative infrequency in the upper interval of the core

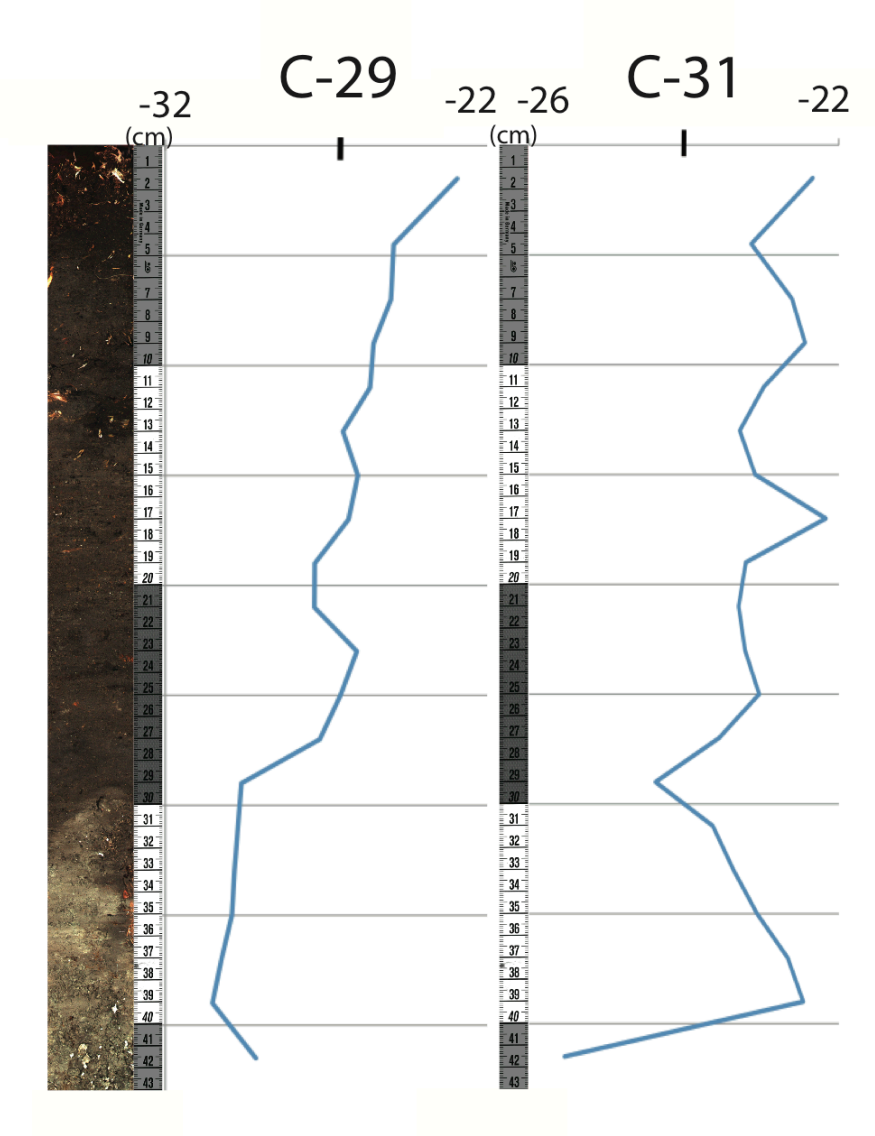

Figure 22. Plot of the n-alkane specific carbon isotope data for C-29 (deciduous trees) and C-31 (grasses) in Core 1A. Both these n-alkanes become more negative up core suggesting more C4 plants and a possible increase in aridity. It is important to remember for this type of test 4 cm of samples had to be combined to produce one one data point. The plots of the other n-alkane lengths can be found in appendix 7. Y-axis is depth in centimeters.

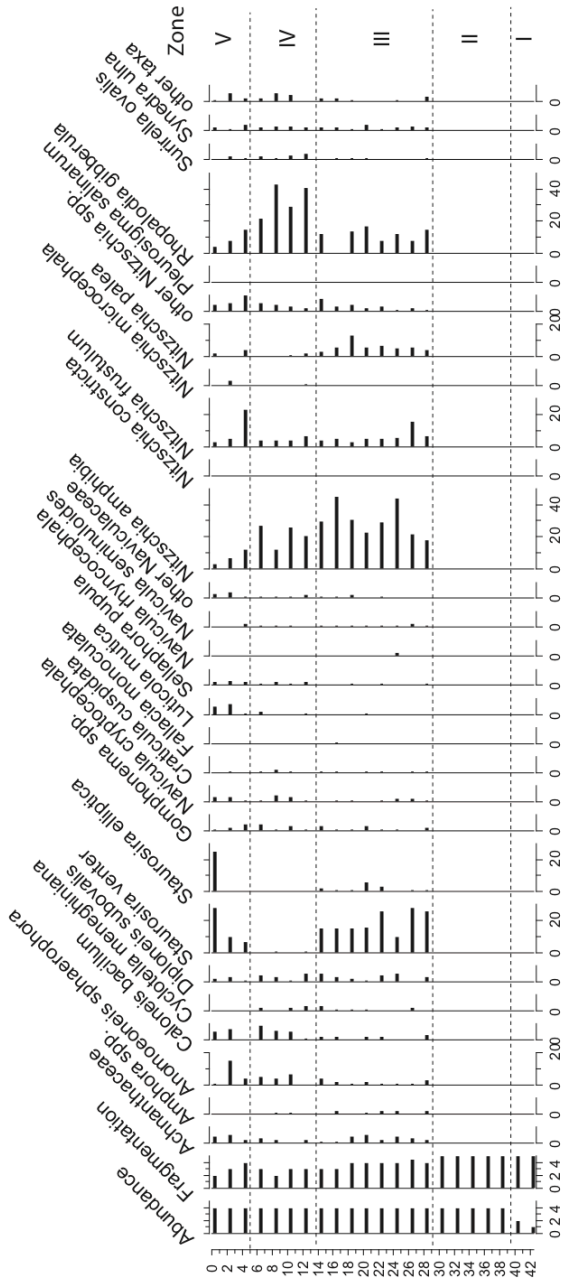

Figure. 23. Diatom analysis performed by Dr. R.B. Owen on Core 1A. Zones I and II contain only fragmented specimen. Zones III and V are dominated by freshwater taxa. Zone IV contains a higher amount of saline-tolerant taxa (Rhopaloda giberula) and a decrease in freshwater taxa (mainly Staurosira verter). Y-axis is depth in centimeters

it is possible some testate amoebae are in the lower interval but were not found during the analysis. Preliminary identification was made with the assistance of Michelle Goman (Figure 24).

Radiocarbon Dating

Radiocarbon Dates

A Conventional Radiocarbon Age of 270 +/- 30 years BP was reported. When calibrated this age corresponds to a 1 sigma age range of Cal AD 1640 to 1650 (Cal BP 310 to 300) and a 2 sigma range of CalAD1520 to 1570 (Cal BP430to 380), CalAD1590 to 1590 (Cal BP360to 360), Cal AD 1630 to 1670 (Cal BP 320 to 280), Cal AD 1780 to 1800 (Cal BP 170 to 160), and Cal AD 1950 to 1950 (Cal BP 0 to 0) (Appendix 8).

A second core, 3C, was also age dated using seeds collected at 28-29 cm depth. A Conventional Radiocarbon age of 10 years +/- 20 years BP suggests either the GWD started fairly recently and sedimentation/deposition rates are extremely high or the sample sent for dating was contaminated with modern material (Appendix 8).

DISCUSSION

Remote Sensing

The NDVI analysis of the northeast margin of Lake Eyasi revealed a belt of vegetation along the northeast lake margin as well as four likely GWD sites all of which were highly vegetated in all images (Fig. 12). While ground-truthing the four GWD sites was not logistically feasible, the consistency of the high amounts of vegetation and lack of visually identifiable surface water source suggests these are GWD associated features. Additionally numerous GWD sites visited during the field season fell within the

Figure 24. Images of testate amoebae identified in Core 1A. All images were taken at the same magnification (40x lens, 10x eyepiece, and slight additional magnification from the camera mount). **Purple area:** Corythion-Trinema type, known for the "overbite," which when viewed from the side looks hook-like (most distinct in the top, left image at the tip of the oval in the upper right corner). **Green area:** possibly Euglypha type (E. rotunda/tuburculata) or Difflugia rubescens, these specimen are plated, possibly toothed or crenulated at the mouth (most distinct in the lower left corner of the top, rightmost image. Far left image shown with diatom for an idea of scale. **Navy blue area:** could be Hyalospheria subflava.

consistently vegetated band identified in the NDVI analysis, suggesting this vegetated band may be groundwater-fed. This idea was further supported by the visual analysis of the higher resolution (less than 2 meters) GoogleEarth imagery, which showed a region along the lake margin with hundreds of GWD sites clustered close together (Fig. 13).

The imagery provided by GoogleEarth does not contain the spectral band data that Landsat imagery contains, limiting GoogleEarth imagery to visual analysis, however there are numerous useful tools, such as the "ruler tool" which aid in the visual analysis. The "ruler tool" was used in this study as a means of determining the approximate sizes of numerous features without having to visit them in the field. When looking at the general size of the GWD features it became apparent why there was only limited success with the Landsat-NDVI study. The majority of GWD features were found to be under 30 m in diameter and located close together. As a result of the lower resolution of Landsat imagery (~30 m), a GWD feature had to be larger than 30 m by 30 m to take up one pixel on the Landsat image. Additionally with low resolution pixels often represent a "mixed" source, for example if one 30 m by 30 m contains vegetation and bare soil it will give a mixed signal over the whole pixel. As a result of mixed pixels the hundreds of small GWD features spaced closely together appear as a region of increased vegetation rather than individual features.

It is possible to identify GWD regions using Landsat imagery though smaller features require imagery with higher resolution. Having access to the higher resolution imagery available through GoogleEarth made it possible to visually confirm identified sites that were inaccessible due to their remote locations. GoogleEarth imagery provides

remarkably detailed images, however unlike Landsat, does not contain spectral band data, thus restricting analysis. Utilizing both data sets allows for a more detailed analysis then the analysis of just one could provide.

Groundwater Discharge Onset

The transition from the lower interval of Core 1A to upper interval, occurring at approximately 30 cm depth, is interpreted as the onset of groundwater discharge to the site. Aside from the obvious visual difference between the lower and upper intervals of the core, numerous other tests revealed additional changes occurring at the transition. Physical analysis of the core revealed higher magnetic susceptibility and density in the lower interval of the core indicating a higher proportion of sediment to organic matter, further supported by the relatively low LOI (percent organic matter) found in the lower interval. High LOI and the geochemical analysis showing both carbon and nitrogen increasing in the upper interval supports the idea that at GWD onset vegetation began growing at the site and has continued growing site since then. There is a relative absence of biological remains (diatoms and testate amoebae) in the lower interval of the core and a sudden appearance of numerous diatom assemblages and testate amoebae after the transition into the upper interval. The changes occurring in these different tests all indicate there was a change in the environment from one with no GWD, unable to support vegetation or organisms, to one where GWD is continual, supporting vegetation and organisms through to the present time.

Seeds collected from just above the transition point, between 28-29 cm depth, produced a conventional radiocarbon age of 270 +/- 30 years BP which calibrates to a range of calendar ages, however all of the dates fall between 497-215 years before today

(2012) placing the onset of GWD between 1515-1797 cal yr AD. Rough estimations were made to determine reasonable travel times for groundwater originating on Mt. Oldeani (Figure 4 and labeled OD in Figure 5) and flowing to the GWD sites and have produced a range of values, a groundwater travel time of roughly 400 years being the most plausible (Appendix 9). Applying this estimation to the range of dates for groundwater onset indicates the groundwater that first reached the site was recharged from precipitation on Oldeani approximately 897-615 years before today (2012) (between 1115 – 1397 cal yr AD).

There are two potential causes, tectonic and climatic, for the onset of GWD at this site. If the cause was tectonic, an earthquake or other tectonic activity occurring between 497-215 years ago could have caused the groundwater flow to be redirected and start discharging at the coring site. Tectonics is a less likely cause because there are numerous GWD sites around two sides of the lake and for a tectonic even to affect each the same and cause a permanent redirection of GW is unlikely, however without age dating multiple GWD sites it is not possible to rule out this cause as Lake Eyasi lies within a rift basin. It is more plausible that a change in climate and rainfall amounts resulted in the onset and continuation of GWD at the site. Based on the age date of GWD onset and the calculated travel time for groundwater from source to site (approximately 400 years), the rainfall recharging the GWD at the site fell on Mt. Oldeani between 1115 – 1397 yr AD.

The time frame during which the groundwater was precipitated coincides with the start of the Little Ice Age (~1250 AD). Numerous studies of lake levels in East Africa have shown the Little Ice Age to be a period of increased rainfall and thus high lake levels (Verschuren, 2000; Verschuren et al., 2001) and initiation of wetlands (Ashley et

al., 2004; Driese et al., 2004). This is in opposition to the Medieval Climate Anomaly, a time of increased temperatures and dry climate (Mohammed et al., 1995; Verschuren et al., 2000). Within the Little Ice Age there were a number of drier periods (1380-1420, 1560-1620, and 1760-1840) that some suggest relate to periods of solar maximum (Verschuren et al., 2004). Others have found connections with recent periods of increased rainfall and solar minimums (Thompson and Hamilton, 1983; Stager et al., 2005). The suspected mechanism between solar radiation levels and rainfall deals with the impact of radiation on higher level convection currents (for example in the troposphere), however research into these theories is relatively new and rapidly progressing (Thompson, 1983; Verschuren et al., 2004; Stager et al., 2005).

Wetland Development

Within the upper interval of Core 1A there is evidence that the amount vegetation increased with time as the groundwater-fed wetland developed with time. This increase in vegetation is indicated by the increase in carbon with time found in both the LOI and elemental study. The percent sand analysis also showed a consistent decrease in sand sized particles starting between 15-14 cm depth. One interpretation of this change in percent sand is that the sudden decrease in larger (sand sized) particles corresponds to when tall plants arrived at the site. Larger particles are often carried closer to the ground by wind and tall plants such as *Typha* could act as a barrier causing large particles to fall out at the edges of the stands of tall plants (Deocampo, 1994).

The increase in the amount of carbon/organic matter in the core and the arrival of tall plants all indicate that after GWD began the vegetation surrounding slowly developed into the highly vegetated wetland seen there today. This idea of wetland development is

consistent with what is observed in the higher resolution GoogleEarth imagery. Looking at the different GWD sites it is possible to see ones that have minimal vegetation, while others have stands of taller plants (*Typha*) and even pooling water.

Sub-Interval of Salinity Increase

Within the upper interval of Core 1A is a "sub-interval" or zone, first identified in the diatom analysis, of increased salinity. During this time, from 16 – 5 cm or roughly 50-150 years ago, saline-tolerant diatom taxa appear and freshwater taxa disappear. At the start of this time percent sand decreases, suggesting the arrival of taller plants. Additionally the TOC/TN ratio indicates this period as a time when the source of the organic matter is slightly more aquatic than the rest of the upper interval of the core.

All indications suggest that this was a time when the environment became more saline and may have been receiving more water. There are a couple options to explain this, first the amount of GWD may have increased, supporting larger forms of vegetation and expanding the wetland, which in doing so reabsorbed salt deposited on the surrounding soil and increasing the salinity within the wetland. Alternatively, this may represent a time of increased rainfall and higher lake levels, which may have introduced salinity to the system through frequent flooding of lake water, or a consistently higher lake level could have caused the saltier groundwater below the lake to be mixed with the fresh groundwater typically flowing to the system.

Future Data

Work on this site is ongoing and future results will help bolster some of the findings presented here. Pollen and phytolyth analyses are already underway by Doris Barboni and will provide additional information regarding: arrival time of onion farming

to the area (and the potential anthropogenic impacts of such), further evidence that this GWD wetland expanded and developed over time, and additional information for the paleoclimate of the region at large through blown in pollen. Additionally as part of this study more age dating will be performed, and the plants growing at and around the site will be better characterized in terms of their isotopic and n-alkane signatures so that the results of those studies can be better constrained.

CONCLUSIONS

The objectives of the study to locate groundwater discharge areas in the Eyasi Basin by remote sensing and to determine the longevity of sites by analyzing the sedimentary record of a core from an active wetland were met. Large GWD features (> 30 m^2) were identified with Landsat imagery, but resolution limitations of Landsat did not allow identification of smaller (< 30 m^2) wetlands. GoogleEarth was found to be useful for locating smaller features, but imagery provided by GoogleEarth does not contain the necessary spectral band data, thus limiting its use to visual analysis. Utilizing both data sets allow for a more detailed analysis than just one could provide.

The seven cores collected from three sites on the lake margin of Lake Eyasi had similar records. Core 1A (43 cm) was representative and revealed stratigraphy comprised of two distinct intervals. The bottom interval was an organic-poor (5%) clay containing minor, abraded and broken microfossils and an average C/N ratio of 11.4 suggesting "lake" sediments. The C/N ratio begins at the bottom with a higher proportion of aquatic plants compared to terrestrial plants and up-section the proportion gradually changes to a higher proportion of terrestrial plants at the top of the interval at ~29 cm. Small-scale

fluctuations in the C/N ratio may reflect repeated lake flooding during the lower interval. Radiocarbon dates of seeds collected at the base of the upper layer are 270 +/- 30 years BP (conventional radiocarbon age) in age.

The upper interval, in contrast, is organic-rich (10-35%) clay, with abundant diatoms and testate amoebae, an average C/N ratio (~14.5) and organic remains (n-alkanes) recording the presence of deciduous trees and grasses. N-alkanes of both plant types become more negative up core suggesting increasing aridity with time, despite the apparently flourishing wetland (increase in both C and N). The rather abrupt change in sediments between the lower and the upper layer is interpreted to result from an increase in groundwater discharge to the site with a sufficient positive water budget to support wetland vegetation. A change in environmental conditions is indicated by sediments between 15-5 cm; a higher proportion of aquatic plants to terrestrial plants, a dramatic decrease in sand, and presence of saline-tolerant diatoms. This interval of increased salinity could have number of causes (1) GWD increased expanding the area of the wetland and salinity increased as salt from the surrounding soil was dissolved, (2) the frequency of lake transgressions increased during this time raising salinity, or (3) GWD decreased and salinity rose due to the high rates of evapotranspiration. The top 4 cm of core represents an environment much like the one observed today, a groundwater fed wetland environment, with standing water in localized areas, with tall sedges being the dominant vegetation.

Without more dates on the Eyasi groundwater-fed wetlands, the reason for the initiation of groundwater flow to the site and the sustained flow for the last few hundred years can only be speculation. However, rough calculations for the time for groundwater

to move from the closest recharge area, Mt. Oldeani, to the site is ~400 years. Solar minima connected with the Little Ice Age have been suggested to have triggered periods of higher rainfall in the region starting >700 years ago (Verschuren et al. 2000). This timing is consistent with the initiation of the wetland at the study site at 1515-1797 cal yr AD if the groundwater takes ~400 years to travel from the recharge area to the study site.

In addition to the scientific gains of this study there is the potential to benefit and aid the people living near these GWD features, relying on them for life-sustaining water for themselves as well as livestock and crops. Through a better understanding of what drives these features, how they form, evolve through time, and how long they last, it may be possible to monitor these features through remote sensing and ensuring they remain able to provide much needed potable water to this region. In the same way people today rely on these GWD features it is also likely that early man relied on similar features when trying to cope with Africa's harsh, ever changing climate. GWD features such as those found along Lake Eyasi may be a modern analogue for similar sites preserved near archeological sites in other parts of East Africa. Such GWD features may help explain how early man was able to migrate out of Africa despite uncertain water supply from the major lakes.

GWD and the wetlands associated with them hold great potential for containing climate record, however much more must could understood about the mechanics behind them, and the environment in which they are found. More in depth research into the groundwater path and geohydrology of this region, a better understanding of the isotopic signature of the C_3 and C_4 plants in this region, as well as a more complete understanding of how these GWD features form and evolve through time is required before one can

begin connecting the event seen in this core to one in the past. This study has shown the critical need for further examination of GWD features in this basin and in similar sites around the world as they represent a highly responsive ecosystem capable of capturing climate changes.

REFERENCES

Alin, S. R., & Cohen, A. S., 2003, Lake-level history of Lake Tanganyika, East Africa, for the past 2500 years based on ostracode-inferred water-depth reconstruction: Palaeogeography, Palaeoclimatology, Palaeoecology, vol. 199, no. 1, p. 31-49.

Ashley, G.M., 2001a, Archaeological Sediments in springs and wetlands. In: Stein, J.K., and Farrand, W.R., (Eds.). Sediments in Archaeological Context. The University of Utah Press

Ashley, G.M., 2001b, Orbital rhythms, monsoons, and playa lake response, Olduvai basin, equatorial East Africa at 1.85-1.75 Ma: Eos, Trans. Am. Geophys. Union, 82, F759.

Ashley, G.M., Mworia, J.M., Muasya, A.M., Owens, R.B., Driese, S.G., Hover, V.C., Renaut, R.W., Goman, M.G., Mathai, S., and Blatt, S.H., 2004, Sedimentation and recent history of a freshwater wetland in a semi-arid environment: Loboi Swamp, Kenya, East Africa: Sedimentology, vol. 51, p. 1-21.

Ashley, G.M., Deocampo, D.M., Kahmann-Robinson, J., and Driese, S.G., 2013, Groundwater-fed wetland sediments and paleosols: It's all about water table. In: New Frontiers in Paleopedology and Terrestrial Paeoclimatology, SEPM Special Publication No. 11.

Baker, B.H., 1986, Tectonics and volcanism of the southern Kenya Rift Valley and its influence on rift sedimentation, in Frostick, L.E., Renaut, R.W., Reid, I., and Tiercelin, J.J. eds., Sedimentation in the African Rifts: Geological Society of London, Special Publication 25, p. 45-57.

Bessems, I., Verschuren, D., Russell, J.M., Hus, J., Mees, F., and Cumming, B., 2008, Palaeolimnological evidence for widespread late 18th century drought across equatorial East Africa: Palaeogeography, Palaeoclimatology, Palaeoecology. 259, 107-120.

Bosworth, W., Strecker, M.R., and Blisniuk, P.M., 1992, Integration of East African paleostress and the present day stress data: implication for continental stress field dynamics: Journal of Geophysical Research.

Canwell, P.A., Eglington, G., Robinson, N., 1987, Lipids of aquatic organisms as potential contributors to lacustrine sediments – II: Organic Geochemistry, v. 11, p. 513-527.

Castañeda, I.S., Werne, J.P., and Johnson, T.C., 2007, Wet and arid phases in the southeast African tropics since the Last Glacial Maximum: Geology, v. 35, no. 9, p. 823-826.

Castañeda, I.S., Werne, J.P., Johnson, T.C., Filley, T.R., 2009, Late Quaternary vegetation history of southeast Africa: The molecular isotopic record from Lake Malawi: Palaeogeography, Palaeoclimatology, Palaeoecology, v. 275, p. 100-112.

Castañeda, I.S., Schouten, S., 2011, A review of molecular organic proxies for examining modern and ancient lacustrine environments: Quaternary Science Reviews, v. 30, p. 2851-2891.

Castañeda, I.S., Werne, J.P., Johnson, T.C., Powers, L.A., 2011, Organic geochemical records from Lake Malawi (East Africa) of the last 700 years, part II: Biomarker evidence for recent changes in primary productivity: Palaeogeography, Palaeoclimatology, Palaeoecology, v. 303, p. 140-154.

Cerling, T., Wang, Y., and Quade, J., 1993, Expansion of C4 ecosystems as an indicator of global ecological change in the late Miocene: Nature, v. 361, p. 344-345.

Charman, Dan J., 2001, "Biostratigraphic and Palaeoenvironmental Applications of Testate Amoebae." Quaternary Science Reviews 20.16-17: 1753-1764.

Collister, J.W., Rieley, G., Stern, B., Eglinton, G., Fry, B., 1994. Compound-specific δ13C analyses from leaf lipids from differing carbon dioxide metabolisms. Organic Geochemistry 21, 619-627.

Crafter, S.A., Njuguna, S.G., and Howard, G.W. (eds.) (1992) Wetlands of Kenya. IUCN, Gland, Switzerland, 183 pp.

Dawson, J. B. (1992). Neogene tectonics and volcanicity in the North Tanzania sector of the Gregory Rift Valley: contrasts with the Kenya sector. Tectonophysics, 204(1), 81-92.

Dawson, J.B., The Gregory Rift Valley and Neogene-Recent Volcanoes of Northern Tanzania. Geological Society Memoir no 33, The Geological Society Publishers, London, (2008) 102 p

deMenocal, P., Ortiz, J., Guilderson, T., Adkins, J., Sarnthein, M., Baker, L., & Yarusinsky, M. (2000). Abrupt onset and termination of the African Humid Period: rapid climate responses to gradual insolation forcing. Quaternary Science Reviews, 19(1), 347-361.

Deocampo, D.M., 1997, Modern sedimentation and geochemistry of freshwater springs: Ngorongoro Crater, Tanzania: unpublished M.Sc. thesis, Rutgers University, 140 p.

Deocampo, D.M., and Ashley, G.M., 1999, Sedimentology, geochemistry, and paleohydrolic potential of groundwater wetlands in East African lacustrine basings: International Union for Quaternary Research, XV Congress, Duban, South Africa, p. 52.

Deocampo, Daniel M. "Sedimentary Processes and Lithofacies in Lake-margin Groundwater-fed Wetlands in East Africa." Sedimentation in Continental Rifts: SEPM Special Publication No. 73 (2002): 295-308.

Deocampo, D.M., 2005, Evaporative evolution of surface waters and the role of aqueous CO2 in magnesium silicate precipitation: Lake Eyasi and Ngorongoro Crater, northern Tanzania: South African Journal of Geology, v. 108, p.493-504.

Driese, S.G., Ashley, G.M., Li, Z., Hover, V.C., and Owen, R.B., 2004, Possible Late Holocene equatorial palaeoclimate record based upon soils spanning the Medieval Warm Period and Little Ice Age, Loboi Plain, Kenya. Palaeogeography, Palaeoclimatology, Palaeoecology, v. 213, p. 231-250.

Ebinger, C., Djomani, Y. P., Mbede, E., Foster, A., & Dawson, J. B. (1997). Rifting Archaean lithosphere: the Eyasi-Manyara-Natron rifts, East Africa. Journal of the Geological Society, 154(6), 947-960.

Eglinton, T.I., and Eglinton, G., 2008. Molecular proxies for paleoclimatology. Earth and Planetary Science Letters 275, 1-16.

Eglinton, G., Hamilton, R.J., 1963. The distribution of alkanes. In: Swain, T. (Ed.), Chemical Plant Taxonomy. Academic Press, pp. 187-217.

Feibel, S.C. 2001. Archaeological sediments in lake margin environments. Pp. 127-148. In J.K. Stein, and W.R. Farrand, eds. Sediments in Archaeological Contexts. University of Utah Press, Salt Lake City.

Folk, R. "L., 1980-Petrology of Sedimentary Rocks." Hemphill, Austin.

Foster, A., Ebinger, C., Mbede, E., & Rex, D. (1997). Tectonic development of the northern Taiizaiiian sector of the East African Rift System. Journal of the Geological Society, 154(4), 689-700.

Frostick, L.E., 1997, The East African Rift Basins. In R.C. Selley (ed.) African Basins. Sedimentary Basins of the World, 3. Elsevier Science B.V. Amsterdam, p. 187-209.

Garcin, Y., Williamson, D., Bergonzini, L., Radakovitch, O., Vincens, A., Buchet, G., Guiot, J., Brewer, S., Mathe, P., and Majule, A., 2007. Solar and anthropogenic

imprints on Lake Masoko (southern Tanzania) during the last 500 years. J. Paleolimnol, 37, 475-490.

Gasse, F., 2000. Hydrological changes in the African tropics since the Last Glacial Maximum. Quaternary Science Reviews. 19, 189-211

Gawthorpe, R.L. and Leeder, M.R., 2000, Tectono-sedimentary evolution of active extensional basins. Basin Research, 12:195-218.

Giger, W., Schaffner, C., Wakeham, S.G., 1980. Aliphitac and olefinic hydrocarbons in recent sediments of Greifensee, Switzerland. Geochimica et Cosmochimica Acta 44, 119-129.

Haack, B. 1996. Environmental Auditing, Monitoring wetland change with remote sensing: An East African example. Environmental Management Vol. 20, No. 3, pp. 411-419.

Hay, R.L., 1976, Geology of the Olduvai Gorge: Berkley California, University of California Press, 203 p.

Heiri, O., Lotter, A.F., and Lemcke, G., 2001. Loss on ignition as a method for estimating organic and carbonate content in sediments: reproducibility and comparability or results. Journal of Paleolimnology. 25, p. 101-110.

Hughes, R.H. and Hughes, J.S. (1992) A Directory of African wetlands, IUCN, Gland/UNEP, Nairobi/WCMC, Cambridge, 820 pp.

Johnson, T.C., Brown, E.T., McManus, J., Barry, S., Barker, P., Gasse, F., 2002, A high-resolution paleoclimate record spanning the past 25,000 years in southern east Africa. Science, vol. 296, p. 113- 132.

Johnson, Cara Roure, Gail M. Ashley, Carol B. De Wet, Rachel Dvoretsky, Lisa Park, Victoria C. Hover, R. Bernhart Owen, and Sally McBrearty. "Tufa as a Record of Perennial Fresh Water in a Semi-arid Rift Basin, Kapthurin Formation, Kenya." Sedimentology 56.4 (2009): 1115-137.

Kiage, L.M., and Liu, K., 2006. Late Quaternary paleoenvironmental changes in East Africa: a review of multiproxy evidence from palynology, lake sediments, and associated records. Progress in Physical Geography, 30, 5, pp. 633-658

Kiage, L.M. and Liu K., (2009) Palynological evidence of climate change and land degradation in the Lake Baringo area, Kenya, East Africa, since AD 1650. Palaeogeography, Palaeoclimatology, Palaeoecology. 279, 60-72.

Kutzbach, J.E., and Street-Perrott, F.A., 1985, Milankovitch forcing of fluctuations in the level of tropical lakes from 18 to 0 kyr BP: Nature, v.317, p. 130-134.

Lamb, H., Darbyshire, I., and Verschuren, D., (2003) Vegetation response to rainfall variation and human impact in central Kenya during the past 1100 years. The Holocene, 13, 2 pp. 285-292

Leakey, M. D. (1971). Olduvai Gorge: Volume 3, Excavations in Beds I and II, 1960-1963 (Vol. 3). Cambridge University Press.

Leakey, M. D., & Hay, R. L. (1979). Pliocene footprints in the Laetolil Beds at Laetoli, northern Tanzania. Nature, 278(5702), 317-323.

Le Gall, B., Nonnotte, P., Rolet, J., Benoit, M., Guillou, H., Mousseau-Nonnotte, M., ... & Deverchère, J. (2008). Rift propagation at craton margin.: Distribution of faulting and volcanism in the North Tanzanian Divergence (East Africa) during Neogene times. Tectonophysics, 448(1), 1-19.

Lewis, D.W. and McConchie, D., 1994. Analytical Sedimentology. Chapman & Hall, New York.

Liutkus, C. M., & Ashley, G. M. (2003). Facies model of a semiarid freshwater wetland, Olduvai Gorge, Tanzania. Journal of sedimentary research, 73(5), 691-705.

MaWaRi.net - Home. Web. 4 Jan. 2011. <http://www.mawari.net/>.

Meyers, P.A., 1997. Organic geochemical proxies of paleoceanographic, paleolimnological, and paleoclimatic processes. Organic Geochemistry. Vol. 27 No 5/6, pp. 213-250.

Meyers, P.A., and Ishiwatari, R., 1993. Lacustrine organic geochemistry – an overview of indicators of organic matter sources and diagenesis in lake sediments. Organic Geochemistry. Vol. 20, NO. 7, pp. 867-900.

McConnell, R. B. (1972). Geological development of the rift system of eastern Africa. Geological Society of America Bulletin, 83(9), 2549-2572.

Mohammed, M.U., Bonnefille, R. and Johnson, T.C. (1995) Pollen and isotopic records in Late Holocene sediments from Lake Turkana, Kenya. Palaeogeagraphy, palaeoclimatology, palaeoecology. 119, 371-383.

Mollel, G. F., Swisher, C. C., Feigenson, M. D., & Carr, M. J. (2011). Petrology, geochemistry and age of Satiman, Lemagurut and Oldeani: Sources of the volcanic deposits of the Laetoli area. Paleontology and geology of Laetoli: Human evolution in context, 99-119.

Nicholson, S. E. (1996). A review of climate dynamics and climate variability in eastern Africa. The limnology, climatology and paleoclimatology of the East African lakes, 25-56.

Nicholson, S.E., 2000. The Nature of rainfall variability over Africa on time scales of decades to millennia. Global and Planetary Change, 26, 137-158.

O'Leary, M.H., 1981. Carbon isotope fraction in plants. Phytochemistry 20, 553-567.

Ozesmi, Stacy L., and Marvin E. Bauer. "Satellite Remote Sensing of Wetlands." Wetlands Ecology and Management 10 (2002): 381-402.

Quade, J., Mifflin, M.D., Pratt, W.L., McCoy, W., and Burckle, L., 1995, Fossil spring deposits in the southern Great Basin and their implications for changes in water-table levels near Yucca Mountain, Nevada, during Quaternary time: Geological Society of America, Bulletin, v. 107, p. 213-230.

Raven, P.H., Event, R.F., and Eichnorn, S.E., 1999, Biology of plants: New York, W>H. Freeman and Company, 875 p.

Renaut, R.W. and Jones, B. (2000) Microbial precipitates around continental hot springs and geysers, In: Microbial Sediments (Eds R. Riding and S. Awramik), pp. 187-195. Springer Berlin.

Ring, U., Schwartz, H. L., Bromage, T. G., & Sanaane, C. (2005). Kinematic and sedimentological evolution of the Manyara Rift in northern Tanzania, East Africa. Geological Magazine, 142(4), 355-368.

Rosen, M.R. (1994) The importance of groundwater in playas: a review of playa classification and the sedimentology and hydrology of playas. In: Paleoclimate and Basin Evolution of Playa Systems. (Ed. M.R. Rosen), GSA Spec. Paper, 289, 1-18.

Rowntree, K. M. (1989). Rainfall characteristics, rainfall reliability and the definition of drought: Baringo District, Kenya. South African Geographical Journal, 71(2), 74-80.

Rucina, S.M., Muiruri, V.M., Downton, L., and Marchant, R., (2010) Late-Holocene savanna dynamics in the Amboseli Dasin, Kenya. The Holocene, 1-11.

Russell, J.M., Johnson, T.C., and Talbot, M.R., 2003. A 725 yr cycle in the climate of central Africa during the late Holocene. Geology, 31, 677-680.

Russell, J.M., Eggermont, H.E., Verschuren, D., 2007. Spatial complexity of Little Ice Age climate in East Africa: sedimentary records from two crater lake basins in Western Uganda. Holocene 17, 183-193.

Russell, J.M., Johnson, T.C., 2007. Little Ice Age drought in equatorial Africa: ITCZ migrations and ENSO variability. Geology 35, 21-24.

Russell, J.M., McCoy, S.J., Verschuren, D., Bessems. I., and Huange, Y., (2009) Human impacts, climate change. And aquatic ecosystem response during the past 2000 yr at Lake Wandakara, Uganda. Quaternary Research, 72, 315-324

Ryner, Maria, Karin Holmgren, and David Taylor. "A Record of Vegetation Dynamics and Lake Level Changes from Lake Emakat, Northern Tanzania, during the Last C. 1200 Years." Journal of Paleolimnology 40.2 (2008): 583-601.

Schefuß, E., Kuhlmann, H. Mollenhauer, G., Prange, M., and Patzold, J., 2011, Forcing of wet phase in southeast Africa over the past 17,000 years. Nature. Vol. 480, p 509-512

Scholz, C.A., Johnson, T.C., Cohen, A.S., King, J.W., Peck, J.A., Overpeck, J.T., Talbot, M.R., Brown, E.B., Kalindekafe, L., Amoako, P.Y.O., Lyons, R.P., Shanahan, T.M., Castañeda, I.S., Heil, C.W., Forman, S.L., McHargue, L.R., Beuning, K.R., Gomez, J., and Pierson, J., 2007. East African megadroughts between 135 and 75 thousand years ago and bearing on early-modern human origins. PNAS, 104, no 42.

Stager, J.C., Ryves., D.B., Cumming, B., Meeker, L., Beer, J., 2005. Solar variability and the levels of Lake Victoria, East Africa, during the last millennium. Journal of Paleolimnology 33, 243-251.

Stager, J.C., Ruzmaikin, A., Conway, D., Verburg, P., and Mason, P.J., 2007. Sunspots, El Nino, and the levels of Lake Victoria, East Africa. Journal of Geophysical Research, v. 112, 1-13

Taylor, R.G., Antonies D. Koussis, and Callist Tindimugaya. ”Groundwater and climate in Africa- a review.” Hydrological Sciences 54.4 (2009): 655-662.

Thompson, K., Hamilton, A.C., 1983. Peatlands and swamps of the African continent. In: Gore, A.J.P. (Ed.), Ecosystems of the World, Mires: Swamp, Bog, Fed, and Moor, Regional Studies. Elsevier, Amsterdam, The Netherlands, pp. 331-373.

Thompson, L.G., Mosley-Thompson, E., Davis, M.E., Henderson, K.A., Brecher, H.H., Zagorodnov, V.S., Mashiotta, T.A., Lin, P.N., Mikhalenko, V.N., Hardy, D.R., and Beer, J., 2002. Kilimanjaro Ice core records: evidence of Holocene climate change in tropical Africa. Science vol. 298, 589-593.

Trauth, M.H., Deino, A.L., Bergner, A.G.N. and Strecker, M.R. (2003) East African climate change and orbital forcing during the last 175 kyr BP. Earth Planet. Sci. Lett., 206, 297-313.

USGS – Landsat Missions. Web. 26 Sept. 2012. < http://landsat.usgs.gov/>

Verschuren, D., Laird, K.R. and Cumming, B.F. (2000) Rianfall and drought in equatorial east Africa during the past 1,100 years. Nature, 403, 410-414.

Verschuren, D. (2001) Reconstructing fluctuations of a shallow East African lake during the past 1800 years from sediment stratigraphy in a submerged crate basin. J. Paleolimnol., 25, 297-311.

Verschuren, D., 2004. Decadal and century-scale climate variability in tropical Africa during the past 2,000 years. In: Battarbee, R.W. (Ed.). Past climate variability through Europe and Africa. Elsevier Paleoenvironmental Research Book Series, Amsterdam.

Williams, L.A.J., 1978 Character of Quaternary volcanism in the Gregory Rift Valley, in Bishop, W.W., ed., Geological Background to Fossil Man: London, Scottish Academic Press, p. 55-70.

Wright Jr, H. E. (1967). A Square-Rod Piston Sampler for Lake Sediments: NOTES. Journal of Sedimentary Research, 37(3).

Appendix 1. Original topographic map.

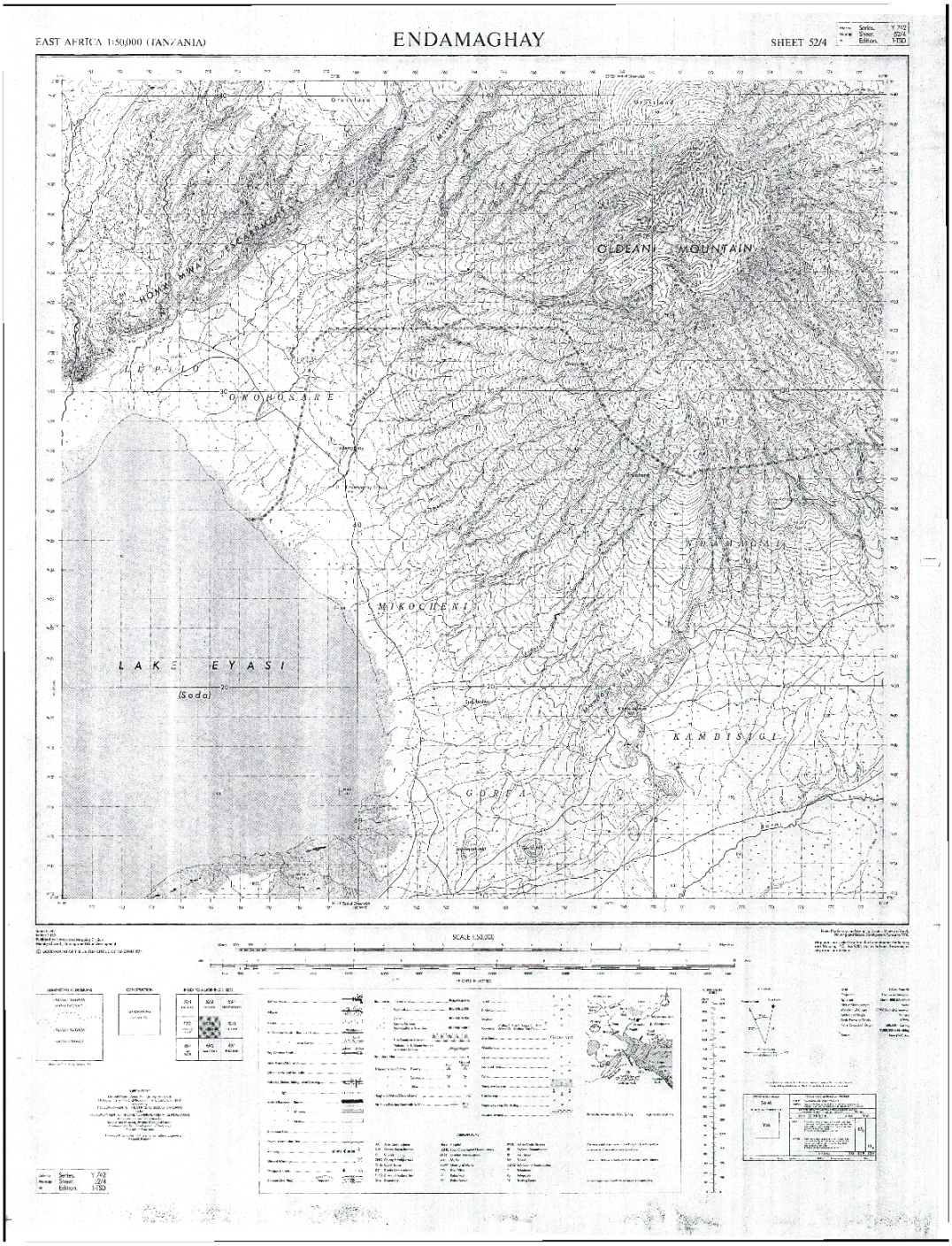

Appendix 2. List of Landsat images available for this study.

Landsat Image Type	Year	Month (Day)	Notes
L7 ETM+SLC - off (2003 - present)			
	2003	Aug. (31)	
	2003	Nov. (19)	
	2003	Dec. (5)	
	2004	Jan. (22)	
	2004	Mar. (26)	clouds
	2004	May (13)	clouds
	2004	May (29)	clouds
	2004	Jun. (14)	clouds, not over site
	2004	Aug. (1)	clouds, not over site
	2004	Sept. (2)	clouds, not over site
	2004	Sept. (18)	clouds, not over site
	2004	Nov. (21)	clouds
	2004	Dec. (23)	clouds
	2005	Jan. (8)	
	2005	Jan. (24)	clouds
	2005	Feb. (25)	
	2005	Mar. (29)	clouds
	2005	Apr. (14)	clouds, not over site
	2005	Aug. (5)	clouds
	2005	Aug. (20)	clouds
	2005	Sept. (5)	clouds
	2005	Sept. (21)	
	2005	Oct. (7)	
	2006	Jan. (27)	clouds
	2006	Feb. (12)	
	2006	Apr. (1)	clouds
	2006	Oct. (10)	clouds
	2006	Oct. (26)	
	2006	Nov. (11)	clouds
	2006	Dec. (13)	clouds
	2007	Feb. (15)	clouds
	2007	Mar. (3)	clouds, not over site
	2007	Mar. (19)	clouds
	2007	Apr. (4)	clouds
	2007	Apr. (20)	clouds
	2007	Aug. (26)	clouds
	2007	Sept. (11)	clouds, not over site
	2007	Sept. (27)	
	2007	Oct. (13)	clouds, not over site
	2007	Oct. (29)	clouds

	2007	Nov. (14)	clouds, not over site
	2007	Nov. (30)	
	2007	Dec. (16)	
	2008	Jan. (1)	clouds, not over site
	2008	Jan. (17)	clouds
	2008	Apr. (6)	clouds
	2008	Apr. (22)	clouds, not over site
	2008	May (8)	clouds, not over site
	2008	Aug. (28)	
	**		
L7 ETM+SLC - on (1999-2003)			
	1999	Sept. (5)	
	1999	Oct. (23)	
	1999	Dec. (10)	
	2000	Jan. (27)	
	2000	Feb. (12)	
	2000	Mar. (31)	clouds
	2000	Apr. (16)	clouds, not over site
	2000	Aug. (6)	clouds, not over site
	2000	Sept. (23)	
	2000	**Oct. (25)**	
	2000	Nov. (26)	clouds
	2000	Dec. (28)	clouds
	2001	Jan. (29)	
	2001	Feb. (14)	
	2001	Apr. (3)	clouds
	2001	Apr. (19)	clouds, not over site
	2001	Sept. (26)	clouds, not over site
	2001	Nov. (13)	clouds
	2002	Feb. (1)	
	2002	Apr. (6)	clouds, not over site
	2002	Jul. (11)	
	2002	Oct. (15)	
	2002	Dec. (2)	clouds
	2002	Dec. (18)	clouds
	2003	Jan. (3)	clouds
	2003	Jan. (19)	
	2003	Feb. (4)	
	2003	Mar. (8)	
	2003	Apr. (25)	
L 4-5 TM			
	1984	Apr. (12)	clouds
	1984	Jun. (15)	clouds
	1984	Jul. (1)	minimal clouds
	1984	Aug. (2)	minimal clouds
	1984	Sept. (3)	minimal clouds
	1984	Nov. (22)	

	1985	Jan. (9)	
	1985	Jan. (25)	clouds
	1985	Apr. (15)	clouds
	1986	May (4)	clouds
	1986	Jul. (23)	clouds
	1986	Aug. (8)	clouds, not over site
	1986	Aug. (24)	clouds
	1986	Oct. (11)	clouds
	1986	Oct. (27)	clouds
	1986	Nov. (12)	clouds
	1986	Nov. (28)	clouds
	1986	**Dec. (14)**	
	1987	Jan. (15)	clouds
	1987	Jan. (31)	clouds
	1995	Jan. (21)	clouds, not over site
	1995	**Feb. (6)**	
	1995	Mar. (26)	clouds
	1995	Apr. (27)	clouds
	2000	Oct. (17)	clouds
	2008	Jun. (17)	clouds
	2008	Sept. (5)	clouds
L 1-5 MSS			
	1972	Nov. (20)	clouds, not over site
	1973	Sept. (4)	clouds
	1973	Sept. (22)	clouds
	1975	Mar. (7)	clouds
	1975	Mar. (25)	clouds
	1975	Apr. (12)	clouds, not over site
	1975	Jun. (5)	clouds, not over site
	1975	Jun. (27)	clouds
	1975	Jul. (29)	clouds, not over site
	1979	Jan. (9)	clouds, not over site
	1979	Jan. (18)	clouds
	1979	Jan. (27)	clouds
	1979	Feb. (5)	clouds
	1979	Feb. (23)	clouds
	1984	Apr. (12)	clouds
	1984	May (30)	clouds
	1984	Jun. (15)	clouds
	1984	Jul. (1)	clouds
	1984	Jul. (17)	clouds
	1984	Aug. (2)	clouds
	1984	Aug. (18)	clouds
	1984	Nov. (6)	clouds
	1984	Nov. (22)	clouds
	1984	Dec. (8)	clouds
	1985	Jan. (9)	clouds, not over site

	1985	Jan. (25)	clouds
	1986	May (4)	clouds
	1986	Nov. (12)	clouds
	1986	Nov. (28)	clouds
	1986	Dec. (14)	clouds, not over site
	1986	Dec. (30)	clouds
	1987	Jan. (15)	clouds
	1987	Jan. (31)	clouds
	1987	Feb. (16)	clouds
	1987	Jul. (10)	clouds, not over site
	1988	Mar. (30)	clouds
	1989	Mar. (1)	clouds, not over site
	1989	Mar. (17)	clouds
	1989	Nov. (28)	clouds
	1990	Feb. (16)	clouds

**Latest images have been removed during USGS site remake.
Bolded images are those used in the NDVI example
Red = cloud free, best images to use
Orange = field area visible but cloud coverage in other part of image, affects some of the analysis, but still usable

Appendix 3. Photographs of all cores collected.

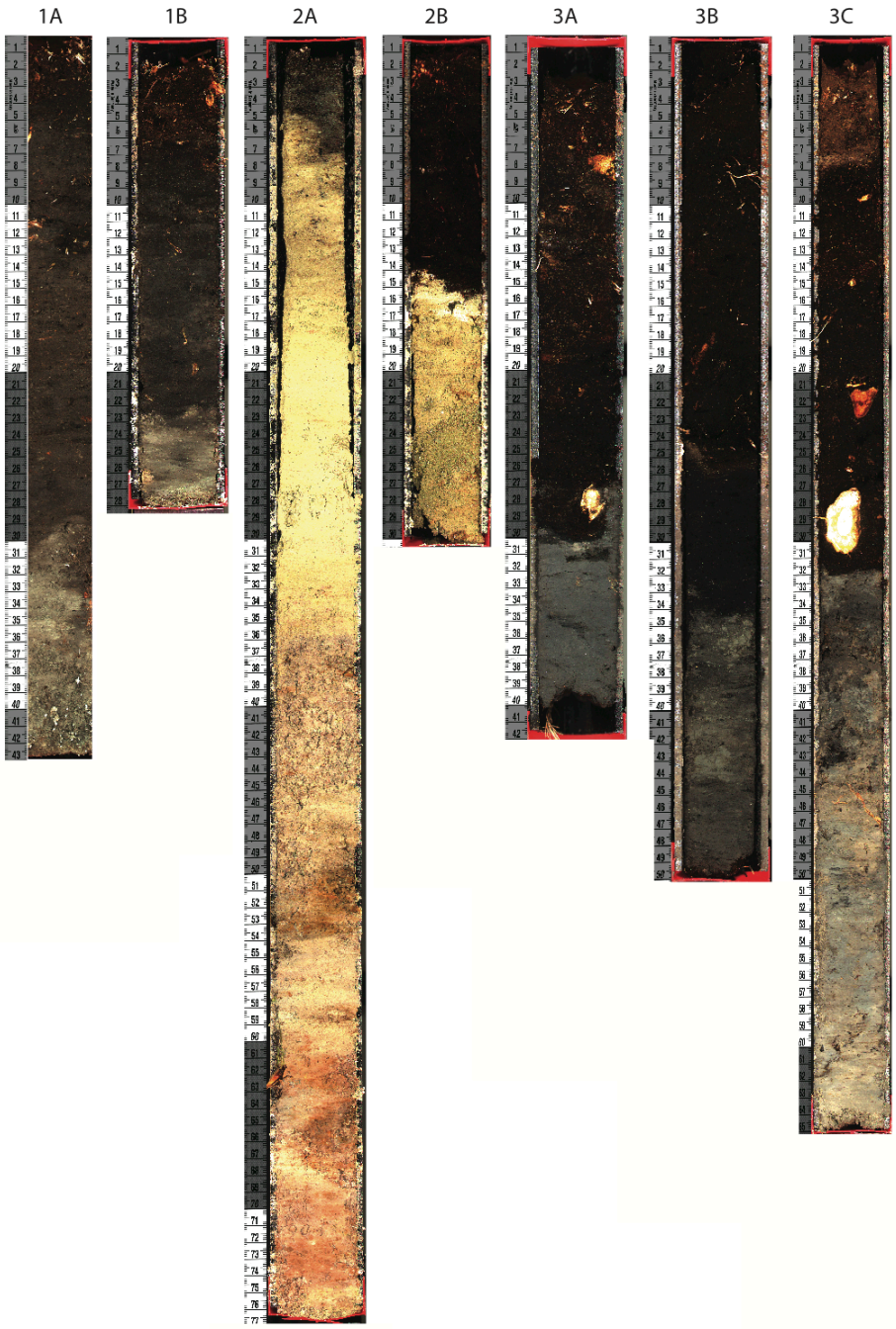

Appendix 4. N-alkane preparation methods.

Short Communication: **Sequential in-cell separation of sedimentary lipids using pressurized liquid extraction.**

Clayton Magill[a1] and Katherine H. Freeman[a]

[a]*Department of Geosciences, Pennsylvania State University, University Park, PA 16802*

[1]*To whom correspondence should be addressed:*

Email: clayton.magill@psu.edu

Phone number: +1 (717) 669-9729

Abstract

A novel method is described for sequential in-cell separation of sedimentary lipids via pressurized liquid extraction (PLE). Total lipid extracts were loaded into PLE cells packed with silica gel, alumina and silver-impregnated alumina and then eluted sequentially with solvent mixtures of increasing polarity to yield four fractions: saturated hydrocarbons, unsaturated/aromatic hydrocarbons, esters/ketones/alcohols and polar compounds including carboxylic acids. Recoveries for target lipids ranged from 74 to 99 %, and were statistically identical to traditional methods (*i.e.*, flash column chromatography) based on gas chromatography–mass spectrometry analysis. Both a standard lipid mixture and more complex sedimentary lipids from wetland soils were separated efficiently, with minimal co-elution among fractions. This study highlights the utility of sequential in-cell separation using PLE for rapid and efficient characterization of sedimentary lipids for environmental and geochemical studies.

Keywords: Soils; Sedimentary lipids; Biomarker; Environmental studies; Pressurized liquid extraction (PLE)

1. Introduction

Biological markers (biomarkers) are a heterogeneous group of organic compounds widely used for environmental and geochemical studies [1]. Biomarkers derive from the biomass of living organisms and are preserved in ancient soils and sediments [2]. Geochemical studies often focus on lipid biomarkers, particularly hydrocarbons such as long-chained *n*-alkanes derived from plant leaves [3], which are both abundant and recalcitrant in sedimentary matrices. However, recent analytical and instrumental advances (*e.g.*, gas chromatography-time-of-flight mass spectrometry) have spurred interest in more functionalized and biologically specific lipid biomarkers, such as dicarboxylic acids from archaea [3] and ω-hydroxyacids from plant roots [4], for example.

Solid-phase extraction (SPE) is a widely used preparative technique that allows for selective analyte isolation and matrix simplification (clean-up) of environmental samples. For over 30 years, SPE has been used to separate target lipids from complex mixtures (see [5] and references therein) by way of stepwise elution over columns with a single stationary phase (*i.e.*, silica gel or alumina). Yet, SPE clean-up is subject to distinct analytical challenges, particularly partial loss of target lipids and co-elution among lipid classes. Using secondary stationary phases during SPE affords enhanced selectivity, but also demands significantly higher sample loads [6], greater solvent volumes and is labor intensive.

Recent studies have adapted PLE techniques to improve analytical efficiency versus SPE by integrating lipid extraction and separation. The exhaustive lipid extraction capabilities of PLE are well established for a spectrum of biological and sedimentary matrixes [7, 8]. Building on this strength, a growing body of work has demonstrated the capability of PLE for selective retention of organic interferences during lipid extraction, resulting in better isolation of target lipids. In particular, these methods add stationary phases (*e.g.*, silica gel) that are homogenized with a sample matrix prior to loading them into PLE cells [9-12]. Parallel developments use multiple mobile phases (*i.e.*, solvents), generally of increasing polarity, to achieve sequential in-cell separation of target analytes [13-16]. Although most applications add a single stationary phase to PLE cells, environmental and geochemical studies often demand multiple-stationary phase separations for adequate isolation of target lipids [17, 18]. Material properties of sample matrices (*e.g.*, leaves *vs.* soils *vs.* marine sediments) vary significantly in environmental and

geochemical studies and can directly influence extraction and separation efficiencies [7, 8]. Multiple-stationary phase in-cell clean-up techniques have been proposed for matrix simplification in the analysis of steroid hormones [19] and polycyclic aromatic hydrocarbons [20], but the utility of adding multiple-stationary phases for sequential in-cell separation of sedimentary lipids remains unclear.

In this study, we present a sequential in-cell separation method for sedimentary lipids that takes advantage of the efficiency, expediency and reproducibility of PLE and the enhanced selectivity (separation power) of multiple solvents over multiple-stationary phases. We first extract lipid biomarkers from sample matrices using PLE, and then separate the resulting total lipid extract (TLE) using stepwise elution over multiple-stationary phases. In adapting PLE for multi-dimensional chromatographic separation, we use a novel cell inversion step and are able yield four lipid fractions separated cleanly both by polarity and unsaturation.

2. Experimental

2.1. Wetland soil samples

Surface wetland soils (A and B_h horizons) were collected from below a shoreline patch of *Carex trisperma* (three-seeded sedge) in an area of bog wetland in central Pennsylvania known as Bear Meadows Natural Area (40.815 °N, 77.925 °W). Sediments were freeze-dried and powdered prior to extraction.

2.2. Reagents and standards

Analytical-grade hexanes (total hexane isomers, 98.5 %,), dichloromethane (DCM, 99.9 %) and methanol (99.8 %) were purchased from EMD Chemicals Inc. (Gibbstown, NJ) and degassed prior to use. Silica gel (60 Å, 70-230 mesh) and neutral alumina (60 Å, 50-150 mesh) were purchased from Mallinckrodt Baker Inc. (Phillipsburg, NJ) and baked for 8 hr at 450 °C. Silver-impregnated alumina (5 % *w*/*w*) was prepared according to reference [21]. Adsorbents were activated for 2 hr at 150 °C prior to use. Pelletized diatomaceous earth (DE) and Ottawa sand were purchased from EMD Chemicals Inc. and baked for 8 hr at 450 °C. Glass microfiber disks served as frits at the top and bottom of PLE cells and came from Whatman International Ltd. (Piscataway, NJ). A standard mixture consisted of the *n*-alkanes C_{15} (nC_{15}) through nC_{22}

plus nC_{29} and nC_{31} (99.0 %; Alfa Aesar, Ward Hill, MA), the saturated hydrocarbons pristane (99 %; Acros Organics, Geel, Belgium) and 5-α-cholestane (99.0 %; Acros Organics), the unsaturated hydrocarbons 1-eicosene (99.0 %; Acros Organics) and squalene (98.0 %; Alfa Aesar), the polyaromatic hydrocarbon (PAH) pyrene (98.0 %; Alfa Aesar), the *n*-alcohols C_{12} ($nC_{12}OH$), $nC_{18}OH$ and $nC_{28}OH$ (98.0 %; Alfa Aesar), the *n*-carboxylic acids C_{16} ($nC_{16}OOH$) and $nC_{26}OOH$ (98.0 %; Alfa Aesar), the *n*-dicarboxylic acid C_{18} ($nC_{18}diOOH$; 98.0 %; Alfa Aesar), benzene-1,2-dicarboxylic acid (commonly called phthalic acid; 98.0 %; Alfa Aesar) and, finally, 2,4-dihydroxybenzoic acid (commonly called α-resorcylic acid; 98.0 %; Alfa Aesar).

2.3. Sample extraction

To generate TLEs, powdered sediments were extracted with DCM/methanol (90:10 *v/v*) using a Dionex ASE 200 system. Either the standard mixture or powdered sediment (about 10 g) was added to cells capped with glass microfiber disks and about 1 g of Ottawa sand. Remaining dead volume was filled with DE/sand (1:1 *v/v*). Cells were extracted in 3 cycles of 5 min at 100 °C and 1500 psi (10.3 MPa) with a flush volume of 70 % [22-24]. Resulting TLEs were blown to dryness under nitrogen and reconstituted in 250 μL of DCM.

2.4. Sequential PLE method

2.4.1. Column construction

Cells were packed as illustrated in Figure 1. Cells were capped with glass microfiber disks and about 1 g of DE/sand (1:1 *v/v*). Then, cells were packed with 1.5 g of silver-impregnated alumina (Ag+alumina), 1.5 g silica gel, 1 g alumina and another 1 g silica gel, respectively. A second glass microfiber disk was added and topped with either the standard mixture or reconstituted TLE. Lastly, cells were packed with an additional 1.5 g silica gel. Remaining dead volume was filled with DE/sand (1:1 *v/v*).

2.4.2. Elution scheme

Ultimately, packed cells were sequentially eluted with hexanes/DCM (95:5 *v/v*) to separate saturated hydrocarbons and hexanes/DCM (70:30 *v/v*) to separate unsaturated/aromatic hydrocarbons. Cells were then *inverted* and sequentially eluted first with 100% DCM to separate

esters/ketones/alcohols and then with the azeotrope methanol/DCM (70:30 *v/v*) to separate polar compounds including oxygen-containing and polyfunctionalized compounds [17, 18]. Elutions proceeded in 3 cycles of 1 min at 50 °C and 500 psi (3.4 MPa) with a total flush volume of 70 %, except for the final elution which occurred at 70 °C. Lipid fractions were blown to dryness under nitrogen and reconstituted in 250 µL of DCM.

2.5. Reference procedures

Sequential in-cell separations were validated with reference to Soxhlet extraction and flash column chromatography [17, 18, 25]. The standard mixture or powdered soil samples (about 10 g) were transferred to cellulose extraction thimbles and Soxhlet extracted with 500 mL of DCM/methanol (90:10 *v/v*) for 18 hr. Resulting TLEs were blown to dryness under nitrogen and reconstituted in 250 µL of DCM.

Reconstituted TLEs were first loaded onto flash columns prepared with 2 g of silica gel [17, 18]. Hydrocarbon, ester/ketone/alcohol and polar compound fractions were eluted with 8 ml of hexanes/DCM (95:5 *v/v*), DCM and methanol/DCM (70:30 *v/v*), respectively. Lipid fractions were blown to dryness under nitrogen and reconstituted in 250 µL DCM. Reconstituted hydrocarbon fractions were further separated on a second flash column prepared with 2 g of Ag+alumina [21]. Saturated hydrocarbons were eluted with 8 mL of hexanes/DCM (95:5 *v/v*) while unsaturated and aromatic hydrocarbons were eluted with 8 mL of hexanes/DCM (70:30 *v/v*).

2.6. Instrumental analysis

Recoveries and separation efficiencies were evaluated using gas chromatography-mass spectrometry (GC/MS). A Hewlett-Packard 6890 Series GC was equipped with a 60 m DB5 fused-silica column (0.32 mm × 0.25 µm) and connected to a Hewlett-Packard 5973 mass selective detector. Reconstituted lipid fractions were injected in splitless mode via a Hewlett-Packard 7683 series autosampler. The GC oven temperature was programmed to 60 °C for 1 min, then ramped to 320 °C at 6 °C min^{-1} and held at final temperature for 20 min. Injector temperature was held at 320 °C. Detector temperature was held at 320 °C. Helium was used as a carrier gas. Functionalized lipids were derivatized using N,O-bis(trimethylsilyl)trifluoracetamide (BSTFA) and detected as trimethylsilyl (TMS) derivatives.

Lipids were identified by comparison with retention times and mass spectra for reference compounds, targeting those in the standard mixture. Peaks were quantified using response factors determined for the standard mixture over a range from 1 to 100 ng μL^{-1}.

3. Theory

3.1. Method development

3.1.1. Column construction and elution scheme

The sequential in-cell separation method developed here builds on established SPE and flash chromatography techniques for separating TLEs with two or more columns [9-20]. Yet, PLE affords sealed cells that can be inverted without compromising column chemistry or integrity, ultimately distilling multiple single-stationary phase columns into a single, multiple-stationary phase column (Figure 1).

Hexanes/DCM (95:5 *v/v*) efficiently eluted only saturated hydrocarbons because silica gel retained the esters/ketones/alcohol and more polar compounds [17, 18, 24] and Ag+alumina retained unsaturated/aromatic hydrocarbon compounds [10]. The second eluent, hexanes/DCM (70:30 *v/v*), eluted unsaturated/aromatic hydrocarbon fractions from Ag+alumina [21, 26], even as silica gel continued to retain esters/ketone/alcohol and polar compound factions [17, 18]. During the second elution step, a hexanes/DCM ratio of 70:30 *v/v* balanced unsaturated/aromatic hydrocarbon recoveries and co-elution versus other hexanes/DCM ratios (*i.e.*, 50:50, 60:40, 80:20 and 90:10 *v/v*).

The relatively low polarity of hexanes/DCM (95:5 *v/v*) and hexanes/DCM (70:30 *v/v*) prevented mobilization of ester/ketone/alcohol and polar compound fractions so that they were retained on silica gel and never reached Ag+alumina. Cell inversion following the second elution step redirected flow and prevented polar compound retention on the transition metal-impregnated adsorbent [27, 28]. Cell inversion also prevented caustic accumulation of transition metals in methanolic fractions [28] because solvated silver is rapidly scavenged by activated alumina [17]. Thus, ‘backflush’ elution over silica gel with DCM and methanol/DCM (70:30 *v/v*) optimized separations ester/ketone/alcohol and polar compound fractions, respectively.

Caution should be exercised when performing sequential in-cell separations using PLE. Assuming conservative lipid holding capacities of about 10 mg g^{-1} for silica gel and alumina [17, 18, 27], the columns described in Section 2.4.1. can handle less than 50 mg lipids. Although sorbent ratios should remain accurate [28], samples of higher lipid contents may require proportionally larger amounts of stationary phases.

3.1.2. Extraction temperature

Higher extraction temperatures generally increase lipid recoveries during solvent extraction, but also decrease separation efficiencies during chromatography [29]. Lipid separations according to unsaturation are particularly sensitive to extraction temperatures because electron donor–acceptor (EDA) complexes formed between unsaturated/aromatic compounds and Ag+alumina typically dissociate between 50 and 100 °C [27, 30]. Extraction temperatures above 100 °C can also result in thermal degradation of lipids [7, 24, 25]. Therefore, lipid recoveries and separation efficiencies were evaluated at 50 to 100 °C in 10 °C intervals. Higher temperatures nominally increased target lipid recoveries, but substantially decreased separation efficiencies. Except for polar compound fractions, extraction temperatures of 50 °C balanced target lipid recoveries and separation efficiencies. Raising temperatures to 70 °C in the final elution step optimized polar compound recoveries.

3.1.3. Extraction cycles, static time and flush volume

Increased extraction cycles, static time and flush volume can increase lipid recoveries [20], but also increase labor and cost. Therefore, target lipid recoveries were evaluated for 1 to 5 cycles of 1 to 10 min static times with 50 to 100 % flush volumes. For 3 cycles of 1 min with 70 % flush volume, target lipid recoveries were comparable to those for 5 cycles of 10 min with 100% flush volume.

4. Results and discussion

4.1. Recovery and separation efficiency

4.1.1. Standard mixture

Under optimized conditions (Section 2.4), sequential in-cell separation of the standard mixture was highly efficient, with fractional recoveries for target lipids of 74 to 99 % (Table 1). Lowest lipid recoveries were associated with polyfunctional (*e.g.*, α-resorcylic acid) and polyunsaturated (*e.g.*, squalene) compounds, although such compounds are often difficult to recover [17, 18, 24, 27].

Overall, lipid fractions in the standard mixture were efficiently separated (Table 1). Saturated hydrocarbon fractions eluted exclusively in hexane/DCM (95:5 *v/v*). Trace amounts of 1-eicosene were also eluted with hexane/DCM (95:5 *v/v*). With the exception of trace amounts of 1-eicosene, and polyunsaturated compounds such as squalene that complex strongly with silver-impregnated stationary phases [27], unsaturated/aromatic hydrocarbons eluted only in hexanes/DCM (70:30 *v/v*). Likewise, ester/ketone/alcohol and polar compound fractions were separated cleanly.

4.1.2. Surface soil samples

The complex nature of soil and other sediments present a challenge when evaluating quantitative lipid recoveries and separation efficiencies. In particular, isomerism can produce unresolved complex mixtures (UCMs) of overlapping peaks in chromatograms. For example, UCMs are apparent in unsaturated/aromatic hydrocarbon and ester/ketone/alcohol fractions of the surface soil samples used for this study (Figure 2). Therefore, separation efficiencies were evaluated qualitatively by monitoring mass chromatograms for individual and combined lipid fractions using selected ions (*m*/*z*) of 85 (major ion of hydrocarbon fragments), 75 (major ion of TMS derivatives), 74 and 103 (major ions of ester/ketone/alcohol TMS derivatives) and 117 (major ion of carboxylic acid TMS derivatives)[1].

Like the standard mixture, sequential in-cell separation of lipid fractions from wetland soils was highly efficient (Figure 2). Hexanes/DCM (95:5 *v/v*) fractions show chromatograms dominated by *n*-alkanes, and *n*-alkane distributions appear identical to those for the TLEs.

Hexanes/DCM (70:30 *v/v*) fractions do not contain traces of *n*-alkanes. BSTFA does not result in discernible differences between derivatized and underivatized mass chromatograms in hexanes/DCM (70:30 *v/v*) fractions, suggesting an absence of functionalized lipids.

Both DCM and methanol/DCM (70:30 *v/v*) fractions show negligible peaks without BSTFA (Figure 2), suggesting that lipids in these two fractions are dominantly functionalized.

However, derivatized DCM fractions show high *m/z* ratios between of 75 and 74 and 103 whereas derivatized methanol/DCM (70:30 *v/v*) fractions show high *m/z* ratios between 75 and 117. This suggests DCM fractions contain ester/ketone/alcohol compounds but methanol/DCM (70:30 *v/v*) fractions contain polar compounds such as dicarboxylic acids.

245

4.2. Comparison between methodologies

Lipid recoveries and separation efficiencies between sequential in-cell (section 2.4) and traditional (section 2.5) separations were compared using the standard mixture based on Student's *t*-test for unpaired values. Calculated *p*-values for target lipids in the standard mixture
250 equaled greater than 0.05 for all fractions (Table 1). Thus, lipid recoveries and separation efficiencies for the two methods were are not different at the 5% significance level.

4. Conclusions

A novel PLE method was developed for sequential in-cell separation of lipid fractions
255 from sedimentary samples. Lipid mixtures were separated cleanly into four fractions based on unsaturation and polarity: saturated hydrocarbons, unsaturated/aromatic hydrocarbons, esters/ketones/alcohols and polar compounds. Lipid recoveries and separation efficiencies for the PLE method compared favorably with traditional methods (*i.e.*, Soxhlet extraction and flash column chromatography), but the PLE method is also automated, reproducible and very efficient.

260

Acknowledgements

This work was supported by NSF grants DGE 0947962 and EAR 9903258. We would like to thank Denny Walizer for laboratory assistance.

References

[1] Peters K, Walters C & Moldowan J (2005) *The Biomarker Guide* (Cambridge University Press).

[2] Kögel-Knabner I (2002) The macromolecular organic composition of plant and microbial residues as inputs to soil organic matter. *Soil Biology and Biochemistry* 34:139.

[3] Castaneda C & Schouten S (2011) A review of molecular proxies for examining modern and ancient lacustrine environments. *Quaternary Science Reviews* 30:2851

[4]Otto A & Simpson M (2006) Sources and composition of hydrolysable aliphatic lipids and phenols in soils from western Canada. *Organic Geochemistry* 37:385.

[5] Poole C (2003) New trends in solid-phase extraction. *Trends in Analytical Chemistry* 22:362.

[6] Bodennec J, *et al*. (2000) A procedure for fractionation of shingolipid classes by solid-phase extraction on aminopropyl cartridges. *Journal of Lipid Research* 41:1524.

[7] Carabias-Martinez R, *et al*. (2005) Pressurized liquid extraction in the analysis of food and biological samples. *Journal of Chromatography A* 1089:1.

[8] Mottaleb M & Sarker S (2012) Accelerated solvent extraction for natural products isolation. *Natural Products Isolation* 864:75.

[9] Huie C (2002) A review of modern sample-preparation techniques for the extraction and analysis of medicinal plants. *Analytical and Bioanalytical Chemistry* 373:23.

[10] Wiberg K, *et al*. (2007) Selective pressurized liquid extraction of polychlorinated dibenzo-*p*-dioxins, dibenzofurans and dioxin-like polychlorinated biphenyls from food and feed samples. *Journal of Chromatography A* 1138:55.

[11] Ong R, *et al.* (2003) Pressurized liquid extraction – comprehensive two-dimensional gas chromatography for fast-screening of polycyclic aromatic hydrocarbons in soil. *Journal of Chromatography A* 1019:221.

[12] Kim J, *et al.* (2003) One-step pressurized liquid extraction method for the analysis of polycyclic aromatic hydrocarbons. *Analytica Chimica Acta* 498:55.

[13] Lundstedt S, *et al.* (2006) Simultaneous extraction and fractionation of polycyclic aromatic hydrocarbons and their oxygenated derivatives in soil using selective pressurized liquid extraction. *Analytical Chemistry* 78:2993.

[14] Poerschmann J & Carlson R (2006) New fractionation scheme for lipid classes based on "in-cell fractionation" using sequential pressurized liquid extraction. *Journal of Chromatography A* 1127:18.

[15] Canosa P, *et al*. (2007) Pressurized liquid extraction with in-cell clean-up followed by gas chromatography-tandem mass spectrometry for the selective determination of parabens and triclosan in indoor dust. *Journal of Chromatography A* 1161:105.

[16] Hussen A, *et al*. (2007) Selective pressurized liquid extraction for multi-residue analysis of organochlorine pesticides in soil. *Journal of Chromatography A* 1152:247.

[17] Bastow T, van Aarssen B & Lang D (2007) Rapid small-scale separation of saturate, aromatic and polar components in petroleum. *Organic Geochemistry* 38:1235.

[18] Still W, Kahn M & Mitra A (1978) Rapid chromatographic technique for preparative separations with moderate resolution. *The Journal of Organic Chemistry* 43:2923.

[19] Hansen M, *et al*. (2011) Determination of ten steroid hormones in animal waste manure and agricultural soil using inverse and integrated clean-up pressurized liquid extraction and gas chromatography-tandem mass spectrometry. *Analytical Methods* 3:1087.

[20] Zhang Q, *et al.* (2012) Determination of polycyclic aromatic hydrocarbons from soil samples using selective pressurized liquid extraction. *Analytical Methods* 4:2441.

[21] Chakraborty K & Raj R (2007) Eicosapentaenoic acid enrichment from sardine oil by argentation chromatography. *Journal of Agricultural and Food Chemistry* 55:7586.

[22] Richter B*, et al.* (1996) Accelerated solvent extraction: a technique for sample preparation. *Analytical Chemistry* 68:1033.

[23] 3545 EM (1995) *Pressurised fluid extraction: test methods for evaluating solid waste* (EPA SW-846).

[24] Wiesenberg G, Schwark L & Schmidt M (2004) Improved automated extraction and separation procedure for soil lipid analyses. *European Journal of Soil Science* 55:349.

[25] Hawthorne S, Grabanski C, Martin E & Miller D (2000) Comparisons of Soxhlet extraction, pressurized liquid extraction, supercritical fluid extraction and subcritical water extraction for environmental solids: recovery, selectivity and effects on sample matrix. *Journal of Chromatography A* 892:421.

[26] Bennett B & Larter S (2000) Quantitative separation of aliphatic and aromatic hydrocarbons using silver ion-silica solid-phase extraction. *Analytical Chemistry* 72:1039.

[27] Cagniant D (1992) *Complexation Chromatography* (CRC).

[28] Christie W (1987) *High-Performance Liquid Chromatography and Lipids: A Practical Guide* (Pergamon Press Oxford).

[29] Haidacher D, Vailaya A & Horvath C (1996) Temperature effects in hydrophobic interaction chromatography. *Proceedings of the National Academy of Sciences* 93:2290.

[30] van Beek T & Subrtova D (1995) Factors involved in the high pressure liquid chromatographic separation of alkenes by means of argentation chromatography on ion exchangers: overview of theory and new practical developments. *Phytochemical Analysis* 6:1.

Figure legends

Fig. 1. Column construction and elution scheme for sequential in-cell separation of lipid mixtures using pressurized liquid extraction. Cells were built from the bottom up using silver-impregnated alumina (Ag+alumina) and activated alumina and silica gel. Lipid mixtures were loaded onto glass microfibers. Dead volume was filled with a mixture of diatomaceous earth (DE) and sand (1:1 *w/w*). Elution with hexanes/DCM (95:5 *v/v*) and hexanes/DCM (70:30 *v/v*) proceeded 'forward,' yielding saturated hydrocarbon and unsaturated/aromatic hydrocarbon fractions, respectively. After cell inversion, elution with DCM and methanol/DCM (70:30 *v/v*) proceeded 'backward,' yielding ester/ketone/alcohol and polar compound fractions, respectively.

Fig. 2. Combined selected ion mass chromatograms (*m/z* 85, 74, 75, 103 and 117) for surface soil total lipid extracts (TLEs) and lipid fractions. The complex nature of surface soil organic matter yielded extensive co-elution during gas chromatography-mass spectrometry analysis (top panel). Lipid fractions were eluted according to polarity and unsaturation via sequential in-cell separation using PLE with hexanes/DCM (95:5 *v/v*, saturated hydrocarbon fractions), hexanes/DCM (70:30 *v/v*, unsaturated/aromatic hydrocarbon fractions), DCM (ester/ketone/alcohol fractions) and methanol/DCM (70:30 *v/v*, polar compound fractions). In the lower panel, relative signal intensity is scaled versus TLEs. Bold chromatograms show derivatized fractions while underlying chromatograms show underivatized fractions. Note that not all target lipids in the standard mixture occur in TLEs. Pr, pristane; Ei, 1-eicosene; Py, pyrene; Di, nC$_{18}$diOOH; Ch, 5-α-cholestane; Sq, squalene.

Appendix 5. Density plots for all cores.

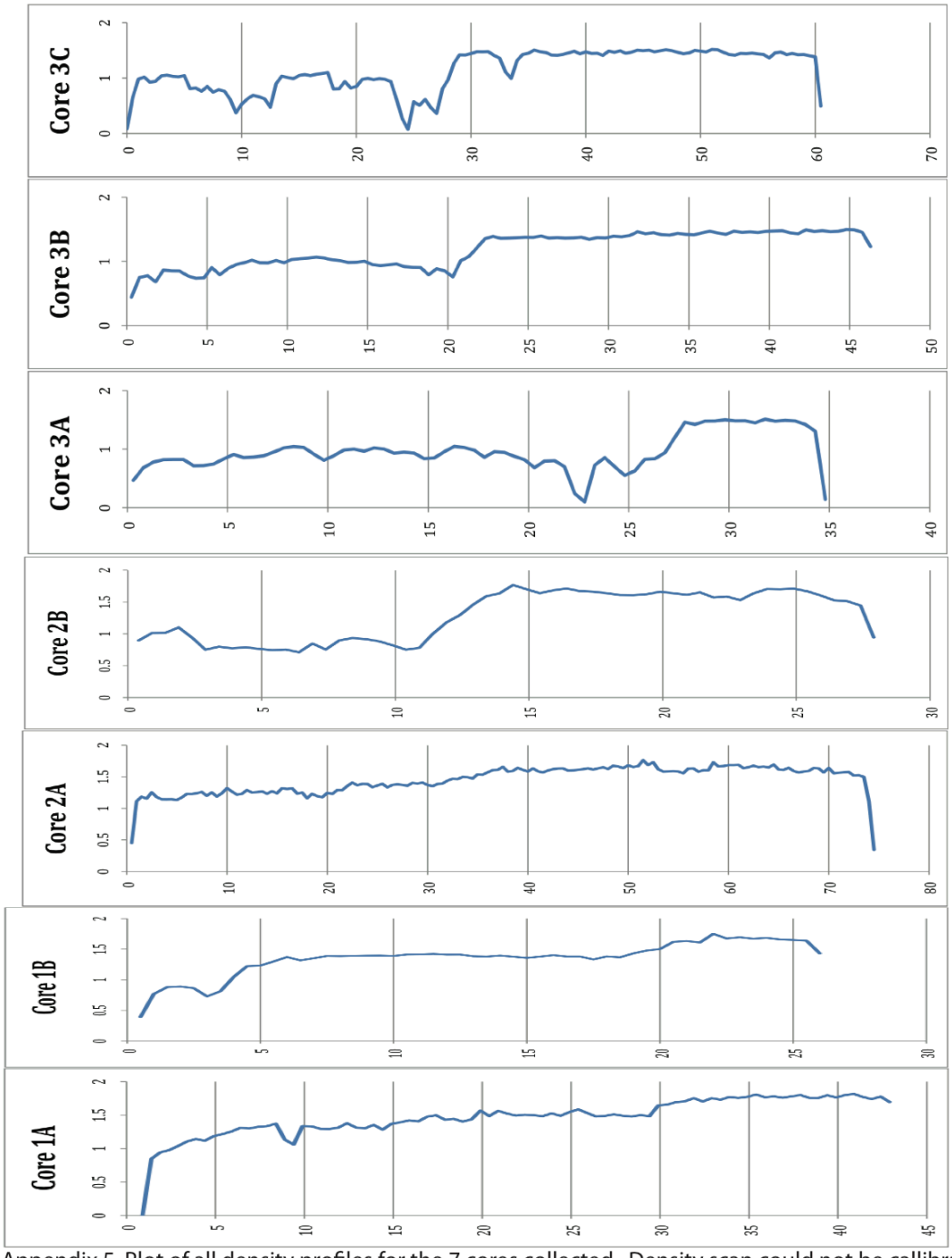

Appendix 5. Plot of all density profiles for the 7 cores collected. Density scan could not be callibrated so the x-axis can only be interpreted in relative and not absolute terms, thus no units have been applied. Y-axis scale is in centimeters. Not the varying scale of X and Y axis between the different graphs.

Appendix 6. Magnetic susceptibility plots for all cores.

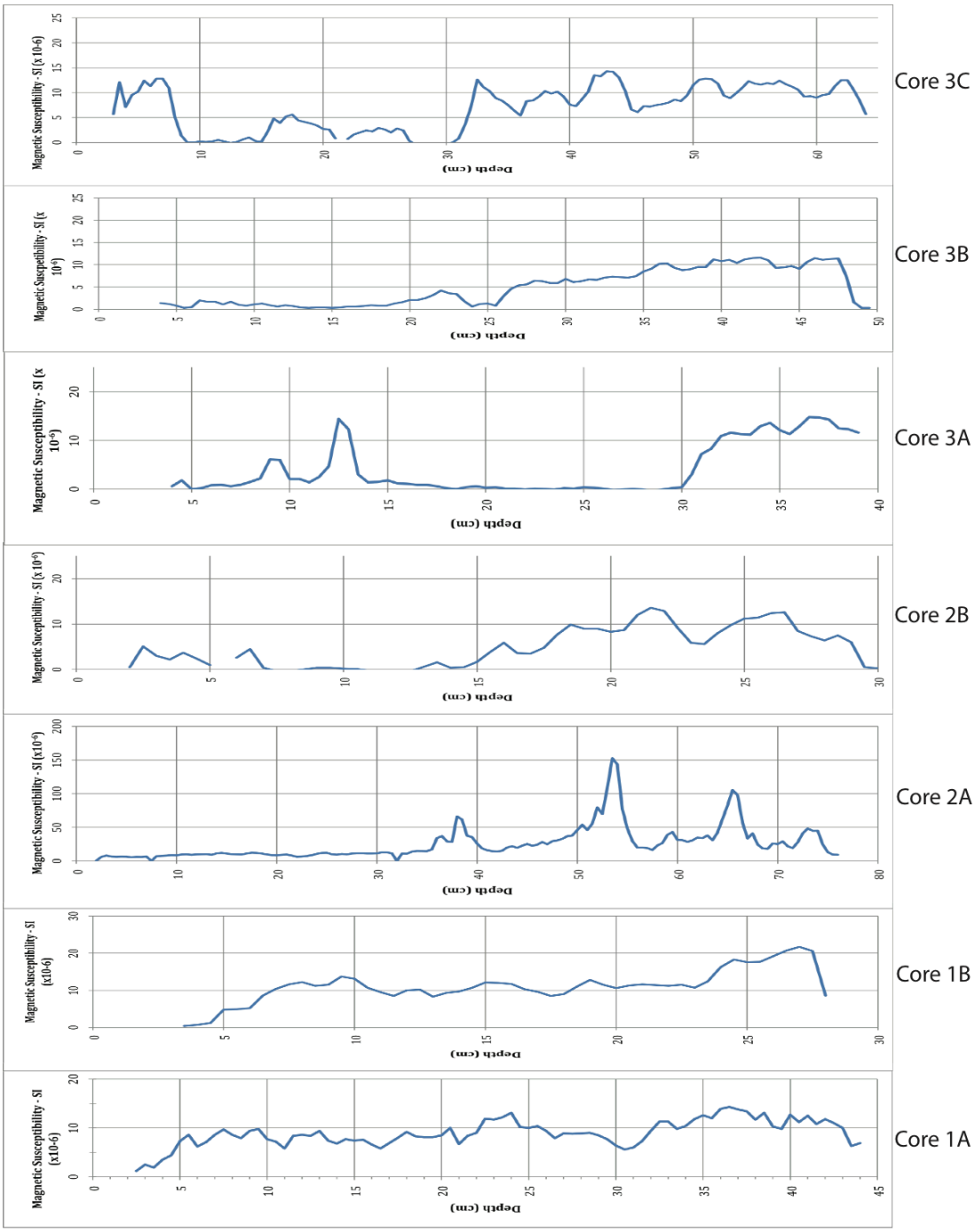

Appendix 6. Magnetic susceptibility plots for all cores collected. Note varying scale on the X and Y axis.

Appendix 7. N-alkane carbon isotope plots for n-alkane chain lengths measured.

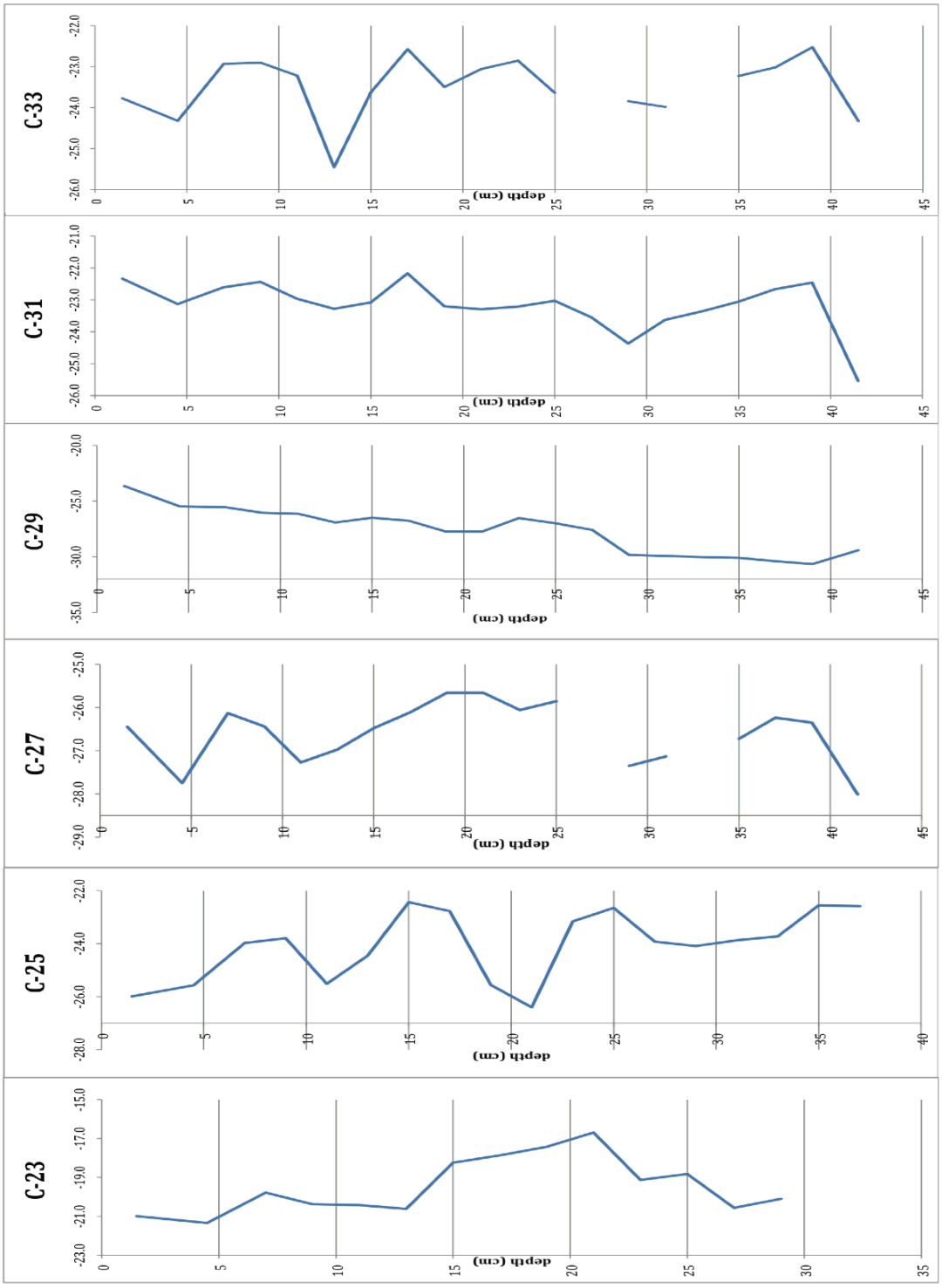

Appendix 8. Radiocarbon Date results for Cores 1A and 3C.

BETA ANALYTIC INC.
DR. M.A. TAMERS and MR. D.G. HOOD
4985 S.W. 74 COURT
MIAMI, FLORIDA, USA 33155
PH: 305-667-5167 FAX:305-663-0964
beta@radiocarbon.com

REPORT OF RADIOCARBON DATING ANALYSES

Ms. Andrea Shilling — Report Date: 7/2/2012

Rutgers University — Material Received: 6/14/2012

Sample Data	Measured Radiocarbon Age	13C/12C Ratio	Conventional Radiocarbon Age(*)
Beta - 323990	NA	NA	270 +/- 30 BP
SAMPLE : 1A.28-29cm			
ANALYSIS : AMS-Standard delivery			
MATERIAL/PRETREATMENT : (seeds): acid/alkali/acid			
2 SIGMA CALIBRATION : Cal AD 1520 to 1570 (Cal BP 430 to 380) AND Cal AD 1590 to 1590 (Cal BP 360 to 360) Cal AD 1630 to 1670 (Cal BP 320 to 280) AND Cal AD 1780 to 1800 (Cal BP 170 to 160) AND Cal AD 1950 to 1950 (Cal BP 0 to 0)			
COMMENT: The original sample was too small to provide a 13C/12C ratio on the original material. However, a ratio including both natural and laboratory effects was measured during the 14C detection to calculate the true Conventional Radiocarbon Age.			
Beta - 323991	60 +/- 30 BP	-28.1 o/oo	10 +/- 30 BP
SAMPLE : 3C.28-29cm			
ANALYSIS : AMS-Standard delivery			
MATERIAL/PRETREATMENT : (seeds): acid/alkali/acid			
2 SIGMA CALIBRATION : Cal AD 1900 to 1900 (Cal BP 50 to 50) and Cal AD Post 1950			

Dates are reported as RCYBP (radiocarbon years before present, "present" = AD 1950). By international convention, the modern reference standard was 95% the 14C activity of the National Institute of Standards and Technology (NIST) Oxalic Acid (SRM 4990C) and calculated using the Libby 14C half-life (5568 years). Quoted errors represent 1 relative standard deviation statistics (68% probability) counting errors based on the combined measurements of the sample, background, and modern reference standards. Measured 13C/12C ratios (delta 13C) were calculated relative to the PDB-1 standard.

The Conventional Radiocarbon Age represents the Measured Radiocarbon Age corrected for isotopic fractionation, calculated using the delta 13C. On rare occasion where the Conventional Radiocarbon Age was calculated using an assumed delta 13C, the ratio and the Conventional Radiocarbon Age will be followed by "*". The Conventional Radiocarbon Age is not calendar calibrated. When available, the Calendar Calibrated result is calculated from the Conventional Radiocarbon Age and is listed as the "Two Sigma Calibrated Result" for each sample.

CALIBRATION OF RADIOCARBON AGE TO CALENDAR YEARS

(Variables: C13/C12=-8.5:lab. mult=1)

Laboratory number: **Beta-323990**

Conventional radiocarbon age: **270±30 BP**

2 Sigma calibrated results: **Cal AD 1520 to 1570 (Cal BP 430 to 380) and**
(95% probability) **Cal AD 1590 to 1590 (Cal BP 360 to 360) and**
Cal AD 1630 to 1670 (Cal BP 320 to 280) and
Cal AD 1780 to 1800 (Cal BP 170 to 160) and
Cal AD 1950 to 1950 (Cal BP 0 to 0)

Intercept data

Intercept of radiocarbon age with calibration curve: Cal AD 1650 (Cal BP 300)

1 Sigma calibrated result: Cal AD 1640 to 1650 (Cal BP 310 to 300)
(68% probability)

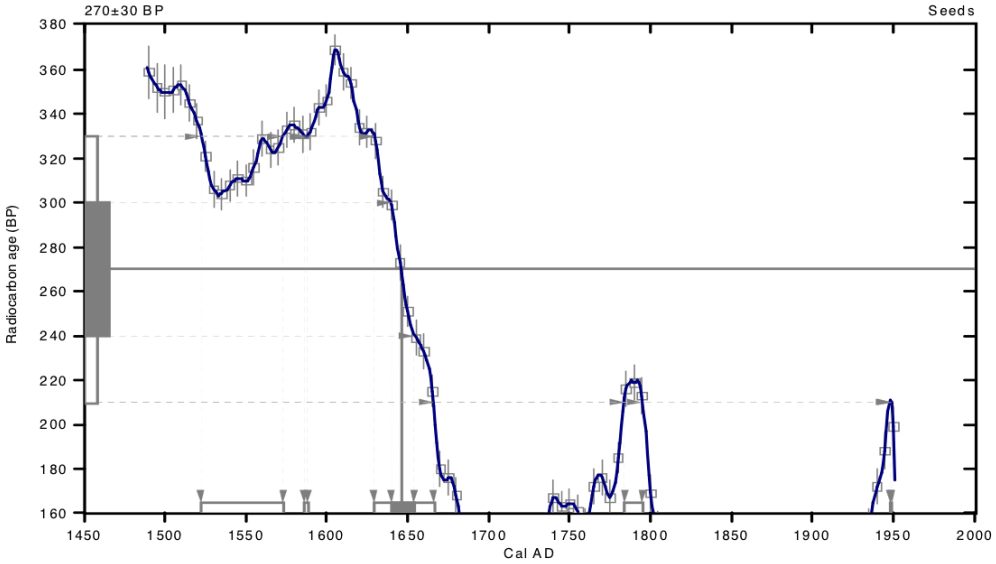

References:

Database used

INTCAL09

References to INTCAL09 database

Heaton,et.al.,2009, Radiocarbon 51(4):1151-1164, Reimer,et.al, 2009, Radiocarbon 51(4):1111-1150, Stuiver,et.al,1993, Radiocarbon 35(1):137-189, Oeschger,et.al.,1975,Tellus 27:168-192

Mathematics used for calibration scenario

A Simplified Approach to Calibrating C14 Dates
Talma, A. S., Vogel, J. C., 1993, Radiocarbon 35(2):317-322

Beta Analytic Radiocarbon Dating Laboratory

4985 S.W. 74th Court, Miami, Florida 33155 • Tel: (305)667-5167 • Fax: (305)663-0964 • E-Mail: beta@radiocarbon.com

CALIBRATION OF RADIOCARBON AGE TO CALENDAR YEARS

(Variables: C13/C12=-28.1:lab. mult=1)

Laboratory number: **Beta-323991**

Conventional radiocarbon age: **10±30 BP**

2 Sigma calibrated results[2]: (95% probability) **Cal AD 1900 to 1900 (Cal BP 50 to 50) and Cal AD Post 1950**

[2] 2 Sigma range being quoted is the maximum antiquity based on the minus 2 Sigma range

Intercept data

Intercept of radiocarbon age with calibration curve: Cal AD Post 1950

1 Sigma calibrated result[3]: (68% probability) Cal AD Post 1950

[3] 1 Sigma range being quoted is the maximum antiquity based on the minus 1 Sigma range

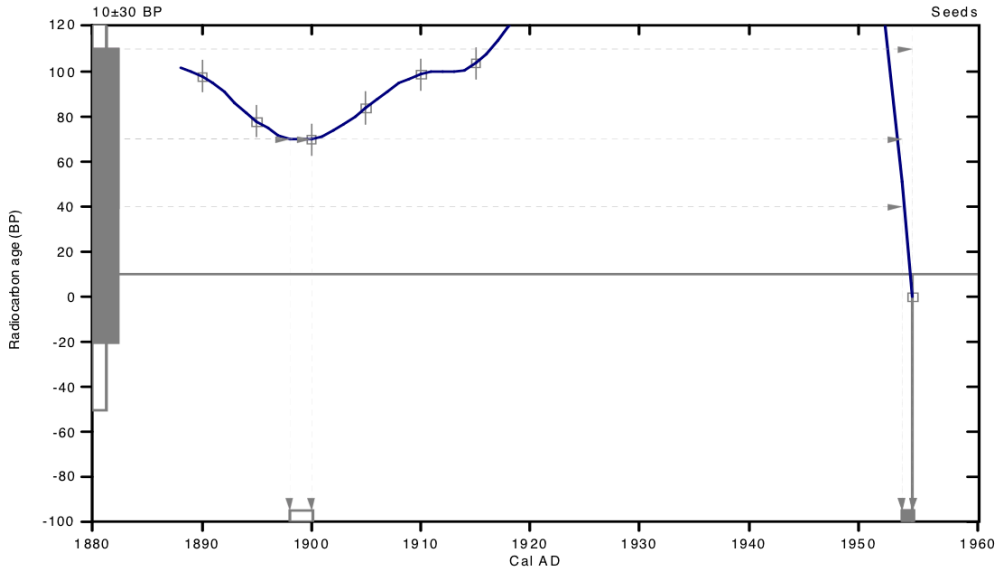

References:

Database used

INTCAL09

References to INTCAL09 database

Heaton,et.al.,2009, Radiocarbon 51(4):1151-1164, Reimer,et.al, 2009, Radiocarbon 51(4):1111-1150, Stuiver,et.al,1993, Radiocarbon 35(1):137-189, Oeschger,et.al.,1975,Tellus 27:168-192

Mathematics used for calibration scenario

A Simplified Approach to Calibrating C14 Dates
Talma, A. S., Vogel, J. C., 1993, Radiocarbon 35(2):317-322

Beta Analytic Radiocarbon Dating Laboratory

4985 S.W. 74th Court, Miami, Florida 33155 • Tel: (305)667-5167 • Fax: (305)663-0964 • E-Mail: beta@radiocarbon.com

Appendix 9. Groundwater travel time calculations.

Oldeani Peak to L. Eyasi Shoreline

Elevation Change (m)	Distance (m) from Google Earth	Area (m2)	k (m2)	K	q secs	q' years	v	Time (Years)
h1-h2	L	A	k		q	q'	v	
2190	21186	1	1.00E-09	9.46E-06	9.78E-07	3.1E+01	1.2E+00	0.81
			1.00E-10	9.46E-07	9.78E-08	3.1E+00	1.2E-01	8.11
			5.00E-12	4.73E-08	4.89E-09	1.5E-01	6.2E-03	162.18
			2.00E-12	1.89E-08	1.96E-09	6.2E-02	2.5E-03	405.46
			1.00E-12	9.46E-09	9.78E-10	3.1E-02	1.2E-03	810.92
			1.00E-13	9.46E-10	9.78E-11	3.1E-03	1.2E-04	8109.21

VALUES USED			EQUATIONS USED
T C	10	Temp	K=k*g*ρ/μ
ρ	0.9997	density	v=q'/n
μ	1.04E-03	viscosity	q=K*(h2-h1)/L specific discharge
			q' is Annual discharge
g	9.81	g	
n	25	porosity	T=1/v
Yr (secs)=	3.15E+07		
v		velocity	

From Gleeson 2011, GRL 38 L02401

k= 2.00E-12 Silty sand to clean sand range of sediments for realistic flow times possibly close to surface

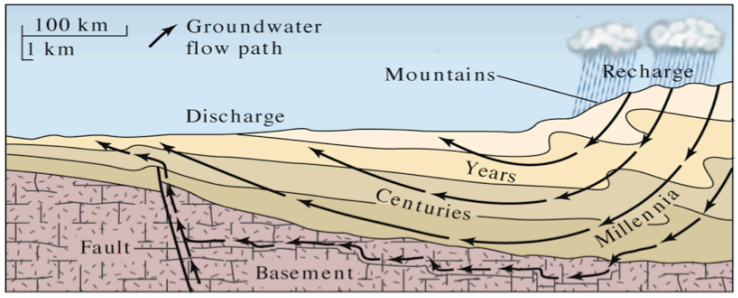

Appendix 9. Upper chart: Basic calculations determining travel time of groundwater from Mt. Oldeani to GWD sites below. Line highlighted in yellow demonstrates most likely groundwater travel time. Lower figure: demonstrating general travel times for groundwater at different depths. Figure from Marshak 2012 Portrait of Earth.